Journal of Rock Mechanics and Geotechnical Engineering 18 (2026) 772–791

Contents lists available at ScienceDirect

Journal of Rock Mechanics and Geotechnical Engineering

journal homepage: www.jrmge.cn

Full Length Article

Multi-physical modeling of climate-driven elasto-plastic deformation, stress redistribution, and water potential in desiccation-cracked soils of arid regions

Milad Jabbarzadeh, Hamed Sadeghi *

Department of Civil Engineering, Sharif University of Technology, Tehran, 1458889694, Iran

ARTICLE INFO

Article history:
Received 11 July 2024
Received in revised form
3 May 2025
Accepted 12 May 2025
Available online 5 August 2025

Keywords:
Soil-atmosphere interaction
Moisture potential dynamics
Stress-deformation characteristics
Desiccation cracks
Arid climate

ABSTRACT

This study presents a multi-physical modeling approach to analyze the dynamics of moisture potential and stress-deformation features near deep desiccation cracks in clayey soils under three consecutive years' climate variability in an arid region. A triple research approach of statistical analysis, analytical framework, and numerical modeling was used to investigate the complex thermo-hydro-mechanical behavior of desiccation-cracked soil, incorporating realistic climatic data of Qom, Iran. The results revealed the interplay between stress, strain, and pore water pressure over time, demonstrating that soil experiences significant swelling and shrinkage due to cyclic wetting and drying. The horizontal stress distribution shows compressive stress concentration at crack tips during wetting, transitioning to tensile stresses uniformly across the soil surface during drying paths. Similarly, vertical stress distributions exhibit localized compressive stresses along crack boundaries during wetting and tensile stresses during drying, highlighting the critical stress conditions at crack tips. The model differentiates between microstructural and macrostructural changes in porosity. Annual trends in micro-porosity revealed cyclic-dependent behavior, with significant volumetric changes occurring in the first year, stabilizing with successive cycles. The results also indicated that part of the volumetric changes are irreversible, with volumetric plastic strain increasing exponentially but at a decreasing rate over three years. Principal stress analysis indicates a shift from compressive to tensile stress states around cracks, driven by climate-induced wetting and drying cycles. These findings underscore the critical role of climate variability in shaping cracked soil behavior in arid regions, providing insights into the heterogeneous behavior of cracked soil surfFicial layers.

1. Introduction

Arid regions experience extreme climatic conditions that significantly affect soil behavior. The soil in these regions often undergoes cyclic wetting and drying due to sporadic rainfall and prolonged dry periods. These climatic conditions contribute to significant soil moisture variations, which in turn lead to volumetric changes in the soil matrix. The process of soil drying and subsequent shrinkage often results in the formation of desiccation cracks, which can penetrate deep into the soil profile (Abu-Hejleh and Znidarčić, 1995). These cracks exacerbate the soil's susceptibility to further volumetric changes and stress alterations, posing challenges for engineering practices.

The mechanism of soil cracking is primarily due to tensile stresses that exceed the soil's tensile strength (Konrad and Ayad, 1997; Tang et al., 2010). However, shear stress-induced soil cracking has also garnered significant interest in previous research (Wei et al., 2016; Li et al., 2022). Cracks create new soil surfaces for moisture and heat exchange with the surrounding atmosphere, accelerating soil evaporation and intensifying soil shrinkage during drying. Similarly, during wetting, infiltration occurs from both the soil surface and the new surfaces created by cracks as preferential pathways. This accelerates the increase in soil moisture and intensifies soil swelling by allowing deeper soil wetting (Sadeghi et al., 2020; Tian et al., 2023; Jabbarzadeh et al., 2024).

* Corresponding author.
E-mail address: hsadeghi@sharif.edu (H. Sadeghi).

Peer review under responsibility of Institute of Rock and Soil Mechanics, Chinese Academy of Sciences.

https://doi.org/10.1016/j.jrmge.2025.05.018

Soil desiccation-crack evolution has been extensively investigated using experimental tools, with many studies employing image processing techniques to capture crack initiation and propagation (Lu et al., 2016; Zeng et al., 2022). Early work by Towner (1987) highlighted the role of soil suction and moisture content in crack initiation and propagation. Subsequent studies, such as those by Fredlund and Rahardjo (1993), provided a framework for understanding the unsaturated soil mechanics involved in desiccation processes. More recently, Tang et al. (2022) used this method and demonstrated that cracks typically form where tensile strain is concentrated. Once a crack forms, the surrounding strain and displacement fields are rapidly redistributed. These new fields then influence the propagation direction of the crack (Mousavi and Jabbarzadeh, 2025). However, field-scale studies have shown that desiccation cracks often initiate and propagate randomly, sometimes extending several meters in depth accompanied with land subsidence (Gambolati and Teatini, 2015), a phenomenon that has been infrequently examined in detail. Nonetheless, the evolution of these cracks driven by the complex interplay between environmental factors and soil heterogeneity was the main focus of field studies (Morris et al., 1992; Yu et al., 2021; Tourchi et al., 2024a).

Numerical modeling approaches have evolved significantly, incorporating advancements in computational methods and multi-physical coupling. More recent efforts by Haghighat et al. (2023) developed a two-dimensional (2D) finite-discrete element method (FDEM) for solid phase deformation and fracturing, and nonlinear Richards' equation for fluid flow. They employed finite volume discretization to solve the fluid dynamics. Guo et al. (2023) developed a new model into discontinuous deformation analysis (DDA) to simulate the complete desiccation process from volume shrinkage to cracking and curling. The model treats evaporation-induced shrinkage and suction-induced tensile failure separately, with soil suction represented as an equivalent attractive force.

Several experimental studies have investigated soil volumetric behavior under wetting-drying cycles (Nowamooz and Masrouri, 2008; Xu et al., 2022). During the drying process, soil shrinkage primarily results from a decrease in macro-pores. Once the shrinkage limit is reached, the internal pore structure continues to adjust, even though the total porosity remains constant (Cuisinier and Laloui, 2005; Tang et al., 2022). In contrast, during the wetting process, both meso- and macro-pores expand, with the latter being more dominant. However, the soil deformation and pore volume evolution during these cycles are not entirely reversible (Wheeler et al., 2003; Tourchi et al., 2024b; Valipour et al., 2024). It was found that the cumulative shrinkage-expansion deformation mainly stems from changes in macro-pore volumes and is dependent on the number of cycles. As the number of wetting-drying cycles increases, the volumetric deformation tends to reach an equilibrium state (Wang and Wei, 2015). Although the hydromechanical behavior of expansive soils is well recognized in previous studies, the influence of deep and wide field-scale cracks on the volumetric dynamics of cracked soil remains unknown.

The stress redistribution in cracked soil has rarely been studied. Wang et al. (2022) employed an extended-FEM method based on the Mohr–Coulomb theory to simulate the stress distribution near soil crack tips. They found that the significant nonuniformity in stress distribution around the crack tip suggests that crack propagation direction is likely controlled by the local area near the tip, characterized by a large stress gradient within a small region. Under shear stress, the major principal stress increases on one side of the crack tip while the minor principal stress decreases on the opposite side. Houcem et al. (2023) investigated desiccation-induced cracking in fine soil grains using a three-dimensional (3D) hydro-mechanical model, focusing on crack growth across soil depth, suction, and tensile stress variations over time. They found that the 3D tensile stress distribution indicates significant tensile stress in regions of the sample that remain uncracked.

Despite the extensive diversity of studies on the volumetric behavior of expansive soils in response to moisture changes, most research has focused on the volumetric behavior of micro and macro soil pores under imposed wetting and drying cycles. Other studies have explored the progression of cracking under different suction paths, while some have developed advanced constitutive models to simulate the behavior of expansive soils. However, there is a lack of comprehensive study that combines realistic field driven mechanisms with numerical modeling to investigate the thermo-hydro-mechanical behavior of soils suffered from deep cracks. Indeed, deep cracks significantly alter the volumetric behavior of soil and change the stress redistribution mechanisms. Furthermore, considering real climate conditions leads to a better understanding and prediction of soil behavior. This is especially important in arid climates, where the potential for crack propagation, coupled with subsidence, increases the risk of instability for surface and subsurface structures (Sadeghi et al., 2023). Therefore, the aim of this research is to examine the multi-physical behavior of expansive soils with tensile cracks under dry climatic conditions, analyzing the time-dependent volumetric behavior and stress redistribution of soil annually.

2. Theoretical considerations and model framework

The primary objective of this study is to elucidate the stress redistribution and volumetric dynamics of a soil experiencing deep desiccation cracks under variable climatic conditions. To achieve this, the finite element program CODE_BRIGHT (Olivella et al., 1996) and thermo-hydro-mechanical modeling was utilized. A multiphase and multispecies approach was adopted, where phases are identified by subscripts (s: solid, l: liquid, g: gas) and species by superscripts (w: water, a: dry air). The primary state variables considered in this study are displacement (u), liquid pressure (P_l), and temperature (T). The dependent variables are calculated from the state variable using the constitutive equations. The unknowns are calculated by numerically solving the system of partial differential equations (PDEs).

2.1. Balance equations

The balance equations for mass, energy, and momentum were developed using a compositional approach (Panday and Corapcioglu, 1989), focusing on species rather than phases. The mass balance for the solid phase is expressed as

$$\frac{\partial}{\partial t}[\rho_s(1-\phi)] + \nabla \cdot (\boldsymbol{j}_s) = 0 \tag{1}$$

where ρ_s is the solid mass density, ϕ is the porosity, and $\boldsymbol{j}_s$ represents the total flux of solids relative to a fixed reference system.

Water within the soil can exist as liquid or vapor. The water mass balance equation, accounting for both phases, is given by

$$\frac{\partial}{\partial t}\left[\left(\omega_l^w \rho_l S_l + \omega_g^w \rho_g S_g\right)\phi\right] + \nabla \cdot \left(\boldsymbol{j}_l^w + \boldsymbol{j}_g^w\right) = f^w \tag{2}$$

where ω is the mass fraction, ρ is the density, S is the saturation degree, $\boldsymbol{j}$ is the total mass flux, and f^w represents the external water sources.

Assuming thermal equilibrium across phases, the energy balance for the porous medium is

$$\frac{\partial}{\partial t}\left[E_S\rho_S(1-\phi)+E_l\rho_l S_l\phi+E_g\rho_g S_g\phi\right]+\nabla\cdot\left(\boldsymbol{i}_c+\boldsymbol{j}_{Es}+\boldsymbol{j}_{El}+\boldsymbol{j}_{Eg}\right)=f^E \tag{3}$$

where E denotes the specific internal energy for each phase, $\boldsymbol{i}_c$ is the conductive heat flux, $\boldsymbol{j}_E$ is the advective energy fluxes, and f^E represents the internal or external energy sources.

Neglecting inertia effects, the momentum balance reduces to the stress equilibrium equation:

$$\nabla\cdot\boldsymbol{\sigma}+\boldsymbol{b}=0 \tag{4}$$

where $\boldsymbol{\sigma}$ is the total stress tensor and $\boldsymbol{b}$ is the vector of body forces.

2.2. Thermal and hydraulic constitutive equations

Heat conduction through the soil was described by Fourier's law:

$$\boldsymbol{i}_c=-\kappa\nabla T \tag{5}$$

where κ is the thermal conductivity, influenced by porosity and saturation. The geometric mean of the thermal conductivity for all phases is given by

$$\kappa=\kappa_s^{1-\phi}\kappa_l^{\phi S_l}\kappa_g^{\phi(1-S_l)}=\kappa_{sat}^{S_l}\kappa_{dry}^{1-S_l} \tag{6}$$

with κ_{sat} and κ_{dry} representing the thermal conductivity under saturated and dry conditions, respectively. The advective flow of liquid and gas is modeled by Darcy's law:

$$\boldsymbol{q}_\alpha=-\frac{\boldsymbol{k}k_{r\alpha}}{\mu_\alpha}(\nabla P_\alpha-\rho_\alpha\boldsymbol{g}) \tag{7}$$

where $\boldsymbol{k}$ is the intrinsic permeability, $k_{r\alpha}$ is the relative permeability, μ_α is the dynamic viscosity, and P_α is the phase pressure ($\alpha = l,g$). Relative permeability for the liquid phase is modeled using the van Genuchten-Mualem model (Mualem, 1976; van Genuchten, 1980):

$$k_{rl}=\sqrt{S_e}\left[1-\left(1-S_e^{1/\lambda}\right)^\lambda\right]^2 \tag{8}$$

where λ is a shape parameter and S_e is the effective saturation defined in terms of the residual liquid saturation (S_{rl}) and the maximum liquid saturation (S_{ls}) as

$$S_e=\frac{S_l-S_{rl}}{S_{ls}-S_{rl}}=\left[1+\left(\frac{P_g-P_l}{P_0\,(\sigma/\sigma_0)}\right)^{\frac{1}{1-\lambda}}\right]^{-\lambda} \tag{9}$$

where P_0 is the air entry value, σ is the surface tension at a temperature T (° C), and σ_0 is the surface tension at a temperature at which P_0 is measured. The relative permeability for the gas phase is determined by

$$k_{rg}=AS_{eg}{}^\lambda \tag{10}$$

$$S_{eg}=\frac{S_g-S_{rg}}{S_{gs}-S_{rg}} \tag{11}$$

where A is a constant; and S_{rg} and S_{gs} are defined as $1-S_{rl}$ and $1-S_{ls}$, respectively.

Non-advective fluxes, such as vapor diffusion, were modeled by Fick's law:

$$\boldsymbol{i}_g^w=-\left(\tau\phi\rho_g S_g D_g^w\boldsymbol{I}\right)\nabla\omega_g^w \tag{12}$$

$$D_g^w=D\left[\frac{(273.15+T)^n}{P_g}\right] \tag{13}$$

where τ is the tortuosity coefficient, D_g^w is the vapor diffusion coefficient, $\boldsymbol{I}$ is the identity matrix, and D and n are model parameters.

2.3. Mechanical constitutive model

In this study, the Barcelona expansive model (BExM) (Alonso et al., 1999) was employed to simulate the significant swelling strains exhibited by expansive soils. The BExM was chosen due to its capability to address the limitations of traditional models that only allow for minor reversible swelling within the elastic range (Gens and Alonso, 1992; Wang et al., 2013; Ghandilou et al., 2023). Expansive clays, however, undergo substantial volumetric changes that are often irreversible, necessitating a more comprehensive modeling approach. A critical aspect of unsaturated expansive soils is the role of microstructural phenomena occurring at the particle level. To develop a model that aligns with the current understanding of these fundamental processes, it is essential to explicitly incorporate microstructural effects into the formulation. The BExM framework effectively integrates these microstructural considerations, which are crucial for capturing the overall behavior of expansive soils. The microstructural pores are assumed to be always saturated, thus Terzaghi's effective stress concept is applicable: changes in suction (s) induce the same volume change as changes in mean net stress (p). The volume strain at this level is reversible (ε_{vm}^e) and independent of macrostructural effects as

$$\mathrm{d}\varepsilon_{vm}^e=\frac{\mathrm{d}e_m}{1+e_m}=\frac{\mathrm{d}(p+s)}{K_m} \tag{14}$$

$$K_m=\frac{\exp[\alpha_m(p+s)]}{\beta_m} \tag{15}$$

where e_m is the microstructure void ratio, K_m is the microstructural modulus, and α_m and β_m are model parameters. The volumetric strain of the macrostructure can be decomposed into elastic and plastic volumetric strains. The elastic volumetric strain of macrostructure (ε_{vM}^e) can arise from changes in stress or suction. This behavior can be expressed as

$$\mathrm{d}\varepsilon_{vM}^e=\frac{\mathrm{d}e_M}{1+e_M}=\left(\frac{\kappa}{1+e_M}\right)\frac{\mathrm{d}p}{p}+\left(\frac{\kappa_s}{1+e_M}\right)\frac{\mathrm{d}s}{s+p_{atm}} \tag{16}$$

where e_M is the macrostructure void ratio; p_{atm} is the atmospheric pressure; and κ and κ_s are the macrostructural elastic compressibility parameters for changes in stress and suction, respectively. Moreover, the plastic volumetric strain of the macrostructure (ε_{vM}^p) results from changes in stress or suction upon reaching the loading-collapse (LC) curve, which serves as the yield surface of the macrostructure. The LC is a yield curve introduced in the BExM that defines plastic deformation resulting from a combination of mechanical load and hydraulic wetting, alongside microstructural elastic deformations that affect the arrangement of the macrostructure. The former can be defined as

$$\mathrm{d}\varepsilon_{vM}^p=\frac{\lambda(s)-\kappa}{1+e_M}\frac{\mathrm{d}p_0}{p_0} \tag{17}$$

where p_0 is the preconsolidation pressure, and $\lambda(s)$ is the slope of

the virgin consolidation line at suction s which is dependent on the slope of the virgin saturated consolidation line ($\lambda(0)$) and model parameters (r and β) as

$$\lambda(s)=\lambda(0)\left[r+(1-r)\mathrm{e}^{-\beta s}\right] \tag{18}$$

The plastic volumetric strain of the macrostructure induced by activating the SI (suction increase) and SD (suction decrease) yield surfaces can also be expressed as

$$\mathrm{d}\varepsilon_{\mathrm{vM}}^{\mathrm{p}}=f_{\mathrm{I}}\mathrm{d}\varepsilon_{\mathrm{vm}}^{\mathrm{e}} \tag{19}$$

$$\mathrm{d}\varepsilon_{\mathrm{vM}}^{\mathrm{p}}=f_{\mathrm{D}}\mathrm{d}\varepsilon_{\mathrm{vm}}^{\mathrm{e}} \tag{20}$$

where f_{I} and f_{D} are micro and macrostructural coupling functions when two SI and SD yield surfaces of the microstructure are activated, respectively.

Two internal variables define the hardening mechanisms in BExM: $\mathrm{d}\alpha_1$ and $\mathrm{d}\alpha_2$. The hardening associated with SI and SD is governed by $\mathrm{d}\alpha_1 = \mathrm{d}\varepsilon^{\mathrm{p}}_{\mathrm{vSI}} + \mathrm{d}\varepsilon^{\mathrm{p}}_{\mathrm{vSD}}$, where $\mathrm{d}\varepsilon^{\mathrm{p}}_{\mathrm{vSI}}$ and $\mathrm{d}\varepsilon^{\mathrm{p}}_{\mathrm{vSD}}$ are the volumetric plastic strains induced by activation of SI and SD, respectively. On the other hand, the LC hardening is governed by $\mathrm{d}\alpha_2 = \mathrm{d}\varepsilon^{\mathrm{p}}_{\mathrm{vSI}} + \mathrm{d}\varepsilon^{\mathrm{p}}_{\mathrm{vSD}} + \mathrm{d}\varepsilon^{\mathrm{p}}_{\mathrm{vLC}}$, with $\mathrm{d}\varepsilon^{\mathrm{p}}_{\mathrm{vLC}}$ denoting the volumetric plastic strain due to activation of LC. The hardening laws are formulated as

$$\mathrm{d}s_{\mathrm{i}}=\frac{K_{\mathrm{m}}\mathrm{d}\alpha_1}{f}=\mathrm{d}s_0 \tag{21}$$

$$\frac{\mathrm{d}p_0^*}{p_0^*}=\frac{(1+e_{\mathrm{M}})\,\mathrm{d}\alpha_2}{\lambda(0)-\kappa} \tag{22}$$

where s_{i} and s_0 are hardening parameters and p_0^* is the saturated preconsolidation pressure. The function f describes the micro-macrostructural coupling and takes distinct forms depending on whether SI is active (f_{I}) or SD is active (f_{D}). The LC yield locus is expressed in a p–q–s diagram as

$$q^2-M^2(p+k_{\mathrm{s}}s)(p_0-p)=0 \tag{23}$$

where M is the slope of the critical state line, k_{s} is the cohesion increase parameter with suction, and p_0 is the preconsolidation pressure which is defined as

$$p_0=p_{\mathrm{c}}\left(\frac{p_0^*}{p_{\mathrm{c}}}\right)^{\frac{\lambda(0)-\kappa}{\lambda(s)-\kappa}} \tag{24}$$

where p_{c} is a reference stress. Non-associative rule is considered for all yield surfaces, and the LC flow rule follows the expression:

$$\gamma q^2-M^2(p+k_{\mathrm{s}}s)(p_0-p)=0 \tag{25}$$

where γ is adopted to predict zero lateral strain along the K_0 stress path. When SI and SD are reached at a mean stress p, a deviatoric stress q, and a suction value s, the direction of plastic strain is given by the flow rule at the image point on the LC yield surface. The coordinates of the image point (p^*,q^*,s^*) are given by

$$p^*=\frac{\eta^2k_{\mathrm{s}}s-M^2p_0}{\eta^2+M^2},\ q^*=\eta(p+k_{\mathrm{s}}s),\ s^*=s \tag{26}$$

where

$$\eta=\frac{q}{p+k_{\mathrm{s}}s} \tag{27}$$

Accordingly, the gradient of the plastic potential function at the image point gives the direction of plastic strain increments.

2.4. Numerical approach

The system of PDEs is solved using a numerical approach that is categorized into two main components: spatial and temporal discretization. The finite element method is employed for spatial discretization, while finite differences are utilized for temporal discretization. The time discretization is linear, and an implicit scheme is implemented that introduces two intermediate time points, $t^{k+\varepsilon}$ and $t^{k+\theta}$, between the initial time t^k and the final time t^{k+1}. Based on the default settings in the FEM program, both ε and θ are typically assumed to be 1.0. Given that the problem is nonlinear, the Newton-Raphson method is adopted to establish an iterative solution scheme.

It is noted that when the solid mass balance is substituted into the other balance equations, the computation of porosity at intermediate points is unnecessary. This is due to the expectation that porosity varies at a slow rate. Consequently, porosity is integrated explicitly, using values at t^k. This assumption simplifies the calculations and enhances the efficiency of the iterative scheme, as the variation of porosity is effectively captured by the solid mass balance equation. After spatial discretization of the PDEs, the residuals for a single finite element can be expressed as follows:

$$\begin{pmatrix}\boldsymbol{r}_u\\ \boldsymbol{r}_{P_{\mathrm{l}}}\\ \boldsymbol{r}_{P_{\mathrm{g}}}\\ \boldsymbol{r}_T\end{pmatrix}=\frac{\mathrm{d}}{\mathrm{d}t}\begin{pmatrix}\boldsymbol{d}_u\\ \boldsymbol{d}_{P_{\mathrm{l}}}\\ \boldsymbol{d}_{P_{\mathrm{g}}}\\ \boldsymbol{d}_T\end{pmatrix}+\begin{pmatrix}\boldsymbol{a}_u\\ \boldsymbol{a}_{P_{\mathrm{l}}}\\ \boldsymbol{a}_{P_{\mathrm{g}}}\\ \boldsymbol{a}_T\end{pmatrix}+\begin{pmatrix}\boldsymbol{b}_u\\ \boldsymbol{b}_{P_{\mathrm{l}}}\\ \boldsymbol{b}_{P_{\mathrm{g}}}\\ \boldsymbol{b}_T\end{pmatrix}=\begin{pmatrix}\boldsymbol{0}\\ \boldsymbol{0}\\ \boldsymbol{0}\\ \boldsymbol{0}\end{pmatrix} \tag{28}$$

where $\boldsymbol{r}$ represents the residuals; $\frac{\mathrm{d}}{\mathrm{d}t}\boldsymbol{d}$ denotes the storage or accumulation terms of mass, momentum, and energy; $\boldsymbol{a}$ can be referred to as conductance or transmissivity terms; and $\boldsymbol{b}$ corresponds to the internal sink/source terms and boundary conditions. After time discretization, the residuals can be expressed in a more compact form:

$$\boldsymbol{r}\left(\boldsymbol{X}^{k+1}\right)=\frac{\boldsymbol{d}^{k+1}-\boldsymbol{d}^k}{\Delta t^k}+\boldsymbol{A}\left(\boldsymbol{X}^{k+\varepsilon}\right)\boldsymbol{X}^{k+\theta}+\boldsymbol{b}\left(\boldsymbol{X}^{k+\theta}\right)=\boldsymbol{0} \tag{29}$$

where k is the time step index; $\boldsymbol{X}=\left[(u_x,u_y,u_z,P_{\mathrm{l}},P_{\mathrm{g}},T)_{(1)},\ldots,(u_x,u_y,u_z,P_{\mathrm{l}},P_{\mathrm{g}},T)_{(n)}\right]$ represents the vector of unknowns, which includes a maximum of six degrees of freedom per node; and $\boldsymbol{A}$ is the conductance matrix. The Newton-Raphson method for solving this nonlinear system of algebraic equations is formulated as follows:

$$\frac{\partial\boldsymbol{r}\left(\boldsymbol{X}^{k+1}\right)}{\partial\boldsymbol{X}^{k+1}}\left(\boldsymbol{X}^{k+1,l+1}-\boldsymbol{X}^{k+1,l}\right)=-\boldsymbol{r}\left(\boldsymbol{X}^{k+1,l}\right) \tag{30}$$

where l denotes the iteration number. In this approach, the standard Galerkin method is utilized with specific modifications to enhance computational efficiency.

The coupling of THM processes is formulated within a multiphysics framework where mass balance, energy balance, and momentum equilibrium equations are fully integrated with constitutive models governing thermal, hydraulic, and mechanical

behaviors. The thermal model incorporates Fourier's law to describe heat conduction, while hydraulic processes involve both Darcy's law for liquid advective flow and Fick's law for non-advective vapor diffusion. The mechanical behavior is represented by the BExM, which accounts for suction-dependent plasticity and stress-strain evolution. These processes interact through key coupling mechanisms: temperature variations influence suction, water retention, and capillary pressure, affecting both hydraulic and mechanical responses; changes in porosity due to mechanical deformation modify permeability and vapor diffusion pathways, altering fluid transport; and stress-induced structural rearrangements along with variations in the degree of saturation impact thermal conductivity, modifying heat transfer properties. By considering displacement, liquid pressure, and temperature as primary state variables, the framework ensures that dependent variables such as porosity, permeability, and saturation evolve consistently with the governing equations and constitutive relationships, providing a robust and coherent representation of soil behavior under THM coupling.

3. Validation of the numerical model

For confirming the accuracy and reliability of the results obtained from models, this section presents the validation of the numerical approach. Therefore, the experimental test of Romero (1999) on swelling pressure was selected as a benchmark for validation, hence the hydromechanical numerical model was conducted in a similar manner. Given the complexities of the numerical model framework and in the absence of all necessary input parameters, such as all hydraulic and mechanical properties of the soil used, some rational assumptions were made. The swelling pressure test is employed as a relevant base to understand the behavior of expansive soils as a material of interest in this study. The native clay soil used by Romero (1999) has two distinct structural levels: a high-density microstructure (dry density of 1.96 mg/cm^3) and a low-density macrostructure (dry density of 1.37 mg/cm^3). Sánchez et al. (2005) also presented a model for swelling soils based on an advanced plastic model for soil that considers two structural levels. The Romero's research was examined within their numerical model and was compared with laboratory results. Thus, the main objective of the simulation in this section is to reproduce the behavior observed during the test by Romero (1999) and the same numerical model by Sánchez et al. (2005). To this end, a numerical analysis was conducted under conditions that replicate the changes in suction in the laboratory while maintaining constant volume in soil sample. The model's initial conditions include an initial suction of 80 MPa and negligible vertical stress. Subsequently, through a wetting path, the suction was reduced to 0.01 MPa. Finally, during the drying process, the suction was increased to 0.4 MPa.

Fig. 1 illustrates the changes in vertical net stress in relation to suction and the results were compared and validated against the original measurements of Romero (1999) and the predictions of Sánchez et al. (2005). As observed, during the wetting phase and the reduction of suction from 80 MPa to 0.01 MPa, the changes in vertical net stress are initially increased and then decreased. Following the wetting scenario, from the beginning of the drying path, as suction rises from 0.01 MPa to 0.4 MPa, the vertical net stress was consistently decreased. Comparison between the results of both studies with those from the developed numerical model, showing a satisfactory match between experimental and numerical results.

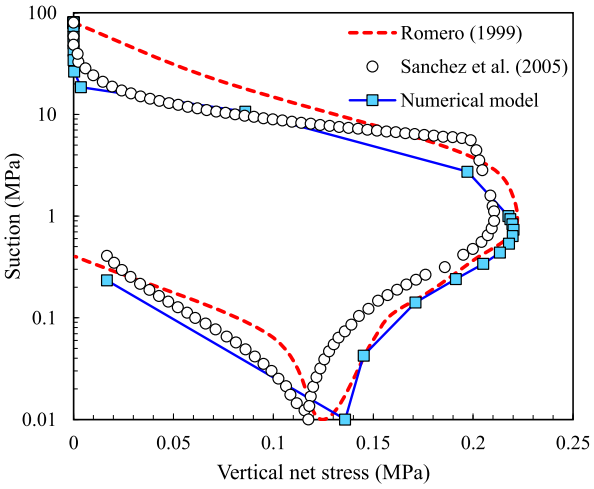

Fig. 1. Comparison of the model results with the measurements from Romero (1999) and the predictions made by Sánchez et al. (2005).

4. General layout and description of the numerical model

The study area in this research is the Qom plain with an arid and semi-arid climate. In this region, deep and wide cracks exist, the main factor of their formation being the phenomenon of desiccation, intensified by various factors such as land subsidence, erosion, and heterogeneous bedrock (Kolahdooz et al., 2020). Fig. 2a illustrates a sample of these observed deep cracks, which are approximately 1 m deep and half a meter wide. However, it is evident that crack depth may vary due to soil erosion during rainfall and flooding events. Naturally, the ratio of crack width to depth, as a dimensionless parameter, follows a specific distribution. Jabbarzadeh et al. (2024) stated that this ratio follows a log-normal distribution. By utilizing this parameter, a wide range of available data in the literature, alongside our field observations, can be utilized. The cracks in the laboratory studies vary on the scale of a few millimeters. However, the cracks observed in the study area are deep and lengthy, posing potential risks to existing infrastructure, such as transmission lines against land subsidence and surface layer shrinkage phenomena (Sadeghi et al., 2024). Therefore, in this study, the crack parameters used in the numerical model, as depicted in Fig. 2b, include crack depth, crack width, and crack spacing.

Cracks have been reported in literature with different depths, for instance, Gambolati and Teatini (2015) referred to cracks with depths of 15–20 m, and Morris et al. (1992) mentioned cracks ranging from 0.5 m to 6 m. However, based on field observations, the cracks present in the field ranged from 1 m to 2 m, which in this study, a crack depth of 1 m was considered in the numerical model. According to Jabbarzadeh et al. (2024), the crack ratio varies from 1% to 42%. Since the cracks observed in this study were approximately half a meter wide and the depth due to soil erosion and filling with soil is not precisely quantified, the crack ratio cannot be explicitly determined. Therefore, in this study, to consider relatively wide cracks, a crack ratio of 35 percent was adopted, meaning a crack width of 35 cm.

The crack formation usually occurs randomly, and cracks have variable distances at the field scale. Hence, in this study, the crack spacing was adopted based on full-scale field observations and complementary statistical analyses. Satellite image, as shown in

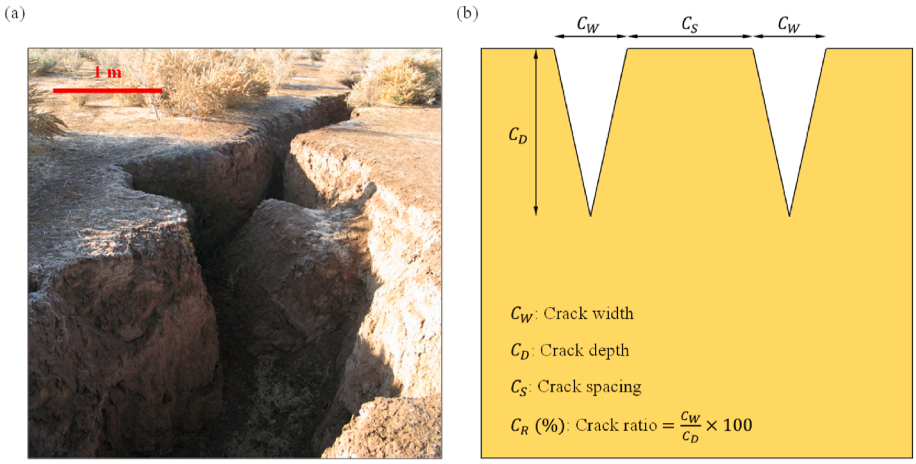

Fig. 2. (a) Observed deep desiccation cracks in the studied area of Qom suburb, Iran; and (b) Schematic diagram of the crack geometry and the corresponding parameters.

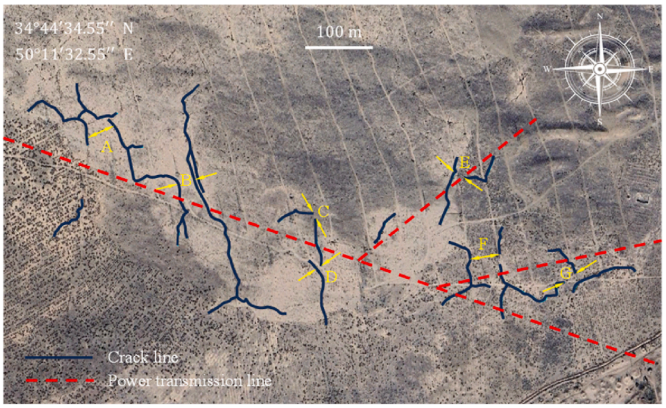

Fig. 3. Satellite image of crack networks in the studied area.

Fig. 3, was used to determine the crack spacing in the studied area. It is evident from this image that these spacings do not follow a specific pattern. It is acknowledged that crack patterns and characteristics are influenced by factors such as soil type, land topography, climatic conditions, and other driving factors for crack formation and propagation along a preferential direction. To identify the crack spacing shown in Fig. 3, seven distances (A to G) were defined. The spacing between cracks was measured, as summarized in Table 1. According to these measurements, the maximum spacing was found at distance A (69.1 m), while the minimum spacing occurred at distance D (11.7 m).

Crack spacing should be defined to preserve the interaction between cracks; otherwise, defining crack spacing adds no value to the analysis and does not differ from modeling a single crack. Therefore, to investigate the impact of crack spacing on findings, initial numerical modeling was required to determine the maximum spacing at which crack interaction is still maintained. As a result, the maximum crack distance was considered to be 10 m. The reason for this is that with greater crack distances, the model geometry becomes more complex, requiring more computational effort without adding significant value. Additionally, based on preliminary numerical models, cracks with greater distances have less interaction with each other and act independently. Furthermore, a minimum distance between cracks of 1 m was considered to ensure that cracks are spaced apart at least by their depth and to avoid numerical divergence as well. Indeed, crack spacing lower than 1 m is unlikely to be observed in field conditions, according to satellite observations.

The random distribution of crack spacing is shown in Fig. 4. For example, the minimum spacing is between the 3rd and 4th cracks which is 1.3 m, and the maximum distance is between the 12th and 13th cracks which is 9.1 m. Therefore, the model geometry comprises 14 cracks with the aforementioned specifications, with a model length of 100 m and a depth of 50 m.

To investigate soil behavior under annual climatic variations, meteorological data for the Qom city was collected over a period of three years from 2015 to 2017 (Jabbarzadeh et al., 2024). These parameters include temperature, precipitation, relative humidity, radiation, and wind speed, whose three-year variations were

Table 1
Crack spacing in the specified zones of the satellite image.

Position	Crack spacing (m)
A	69.1
B	33.9
C	12.4
D	11.7
E	24.5
F	63.5
G	27.8

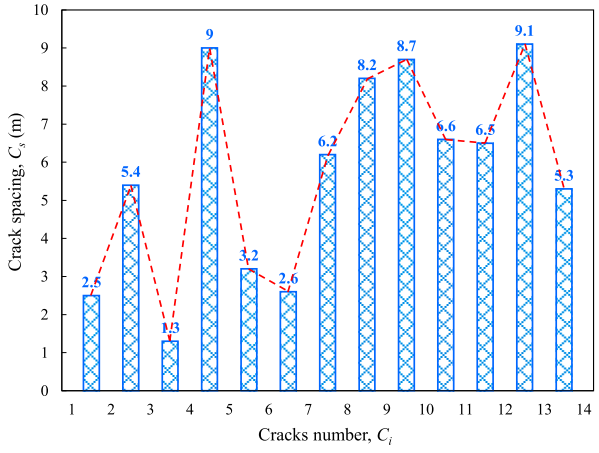

Fig. 4. Random generated distance between cracks.

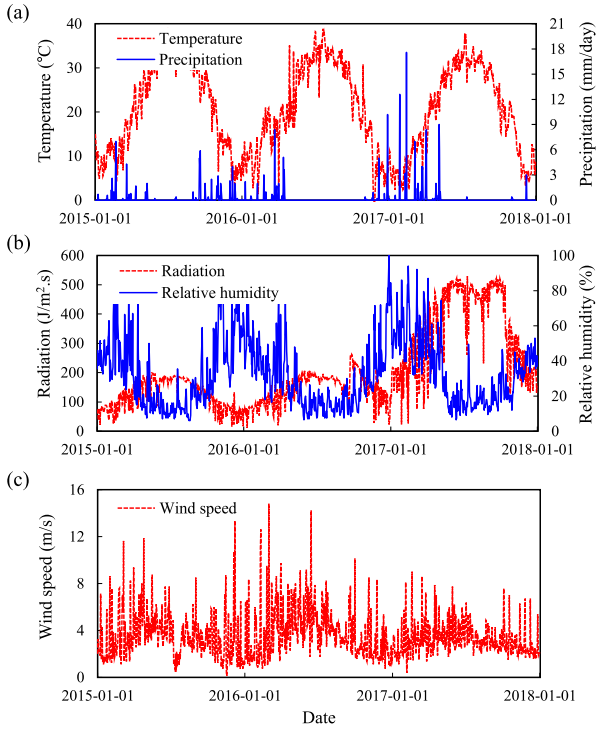

Fig. 5. Meteorological data for Qom city: (a) Temperature and precipitation, (b) Radiation and relative humidity, and (c) Wind speed.

depicted in Fig. 5. For simplification, these values were uniformly applied as atmospheric boundary conditions to the soil surface and crack walls. Since cracks were assumed to be wide, the atmospheric conditions within the crack interior environment can be assumed to be the same as the atmospheric conditions outside, disregarding phenomena such as air circulation within the crack interior environment.

As expansive soils are sensitive to moisture changes and exhibit high cracking susceptibility during wetting and drying cycles, in this study, the Boom clay was used to simulate the cyclic behavior of expansive soils under actual climatic variations. This soil is extensively studied, and its thermo-hydro-mechanical parameters are available in literature (Delage et al., 2000; Dehandschutter et al., 2005; Gens et al., 2011; Bernier et al., 2007; François et al., 2009). The soil properties used in the numerical model were presented in Tables 2 and 3.

As an initial boundary condition for the numerical model, an initial stress of 1 kPa was uniformly applied to the entire model domain as compressive stress. In this study, the compressive stresses are represented with negative signs and tensile stresses with positive signs. The initial porosity and micro-porosity of the soil were assumed to be 0.487 and 0.18, respectively (Delage et al., 2000; Sánchez et al., 2005; Bernier et al., 2007).

Based on field reports from the Qom plain, the groundwater level is reported to be deep, approximately 90 m below the ground surface (Jabbarzadeh and Sadeghi, 2024). In this study, assuming a depth of 90 m for the groundwater level, a hydrostatic boundary condition will be applied as the underlying boundary of the model, with an initial suction of 0.4 MPa. Considering the arid climate of Qom, the presence of deep cracks in the model, and the use of a soil with low permeability, an initial suction of 10 MPa was assumed at the soil surface and crack walls, following a bi-linear distribution of pore water pressure from the groundwater surface to the soil surface.

According to the studies of De Bruyn and Labat (2002), the initial temperature of the Boom clay at a depth of 223 m was reported to be 16.6 °C. In this model, an initial soil temperature of 15 °C was assumed, which changes with climatic variations through thermal conduction mechanisms. Finally, the final model geometry along with the finite element mesh was depicted in Fig. 6. As indicated, the model mesh comprises 7245 constant strain triangle elements and 3954 nodes. Fig. 7 summarizes the general flow of the numerical model and fundamental processes along with the derivation of the geometrical model.

It is important to mention that this study focuses on the behavior of a soil with stabilized desiccation cracks subjected to cyclic wetting-drying conditions. While the propagation of cracks and the formation of new ones are not modeled, the proposed approach only simulates changes in the internal area of stabilized cracks caused by variations in crack width and wall movement due to climate dynamics. As a result, this study highlights the stress redistribution and deformation around existing cracks, assuming that crack propagation within the three-year time span considered is quite marginal hence negligible.

5. Interpretation of the results

5.1. Dynamics of moisture potential and cyclic deformation of the cracked soil

To examine the changes in pore volume, total porosity and micro-porosity against cyclic variations in pore water pressure between 3rd and 4th cracks (the closest cracks) are shown in

Table 2
The thermo-hydraulic parameters of the numerical model (Alonso et al., 1999; Delage et al., 2000).

Parameter	Description	Value
P_0	Measured P at certain temperature (MPa)	3.44
σ_0	Surface tension (N/m)	0.072
λ	Shape function for retention curve	0.3
S_{rl}	Residual saturation	0
S_{ls}	Maximum saturation	1
k_0	Intrinsic permeability (m^2)	2.5×10^{-19}
λ	Model parameter	0.3
A	Constant parameter	1
λ	Model parameter	3
D	Model parameter (m^2 Pa s^{-1} K^{-n})	5.9×10^{-6}
n	Model parameter	2.3
τ_{au}	Coefficient of tortuosity	1
κ_{dry}	Thermal conductivity of the dry porous medium (W/(m K))	0.646
κ_{sat}	Thermal conductivity of the water saturated porous medium (W/(m K))	1.4396

Table 3
Input parameters of the mechanical constitutive model (Sánchez et al., 2005).

Parameter	Description	Value
κ^{Macro}	Matrix elastic stiffness parameter at macro level for changes in mean stress (p)	0.02
κ^{micro}	Matrix elastic stiffness parameter at micro level for changes in mean effective stress $\left(p + s^{micro}\right)$	0.1
κ_s	Elastic macro stiffness parameter for changes in macro suction (s^{macro})	0.01
ν^M	Poisson's ratio	0.3
K_{min}^{Macro}	Minimum bulk modulus at macro level (MPa)	0.001
K_{min}^{micro}	Minimum bulk modulus at micro level (MPa)	0.001
f_{sd0}	Micro and macrostructure coupling functions when SD is activated	−0.1
f_{sd1}	Micro and macrostructure coupling functions when SD is activated	1.1
n_{sd}	Micro and macrostructure coupling functions when SD is activated	2
f_{si0}	Micro and macrostructure coupling functions when SI is activated	−0.1
f_{si1}	Micro and macrostructure coupling functions when SI is activated	1.1
n_{si}	Micro and macrostructure coupling functions when SI is activated	0.5
M	Slope of the critical state line	1
r	Coefficient describing the change in cohesion with suction	0.78
β	Coefficient describing the change in cohesion with suction (MPa^{-1})	5
p_c	Reference pressure (MPa)	0.01
k_s	Coefficient describing the increase of tensile strength with suction	0
p_{t0}	Cohesion corresponding to suction equal to zero (MPa)	0.01
p_0^*	Preconsolidation mean stress for saturated soil (MPa)	0.11
ω	Coefficient of nonassociativity	1
$\lambda(0)$	Slope of the virgin loading line in the e-ln(p) diagram	0.65

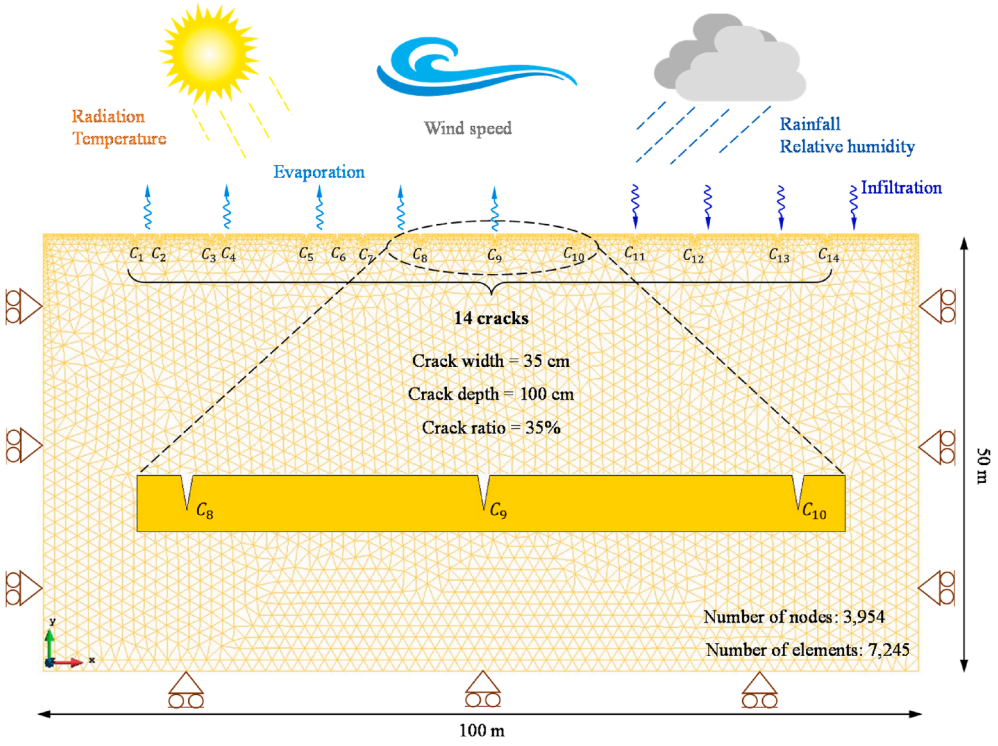

Fig. 6. Finite element mesh and geometry of the numerical model with atmospheric and mechanical boundary conditions.

Fig. 8a. As observed, the trends clearly shift leftward annually along the total porosity axis, indicating increased desiccation of the cracked soil surface and intensified volume reduction each year. Fig. 8b separately illustrates the variations in micro-porosity relative to suction. This figure selectively shows micro-porosity on a specific day from each of the three years, with suction levels of 50, 100, and 150 MPa, respectively, to more clearly examine the annual trends and the suction dependency. The results indicate that with an increase in suction from 50 MPa to 150 MPa, micro-porosity decreases from 0.126 to 0.067 in the first year. In addition to the suction dependency, micro-porosity variations are also time-dependent, demonstrating that in the third year, it changes with a different intercept on the y-axis. While the slope of changes in all three trends remains nearly constant, the y-intercept of micro-porosity changes shifts downward by 0.026 from the initial state to the first year, 0.015 from the first year to the second year, and 0.014 from the second year to the third year. This also indicates that the range of changes in soil pore volume is greater in the first year and decreases with successive seasonal changes due to a tendency towards equilibrium state. Similarly, Fig. 8c shows the changes in total porosity at the same selected suction levels.

The 2D distribution of micro-porosity on days 52 (after 7 mm/

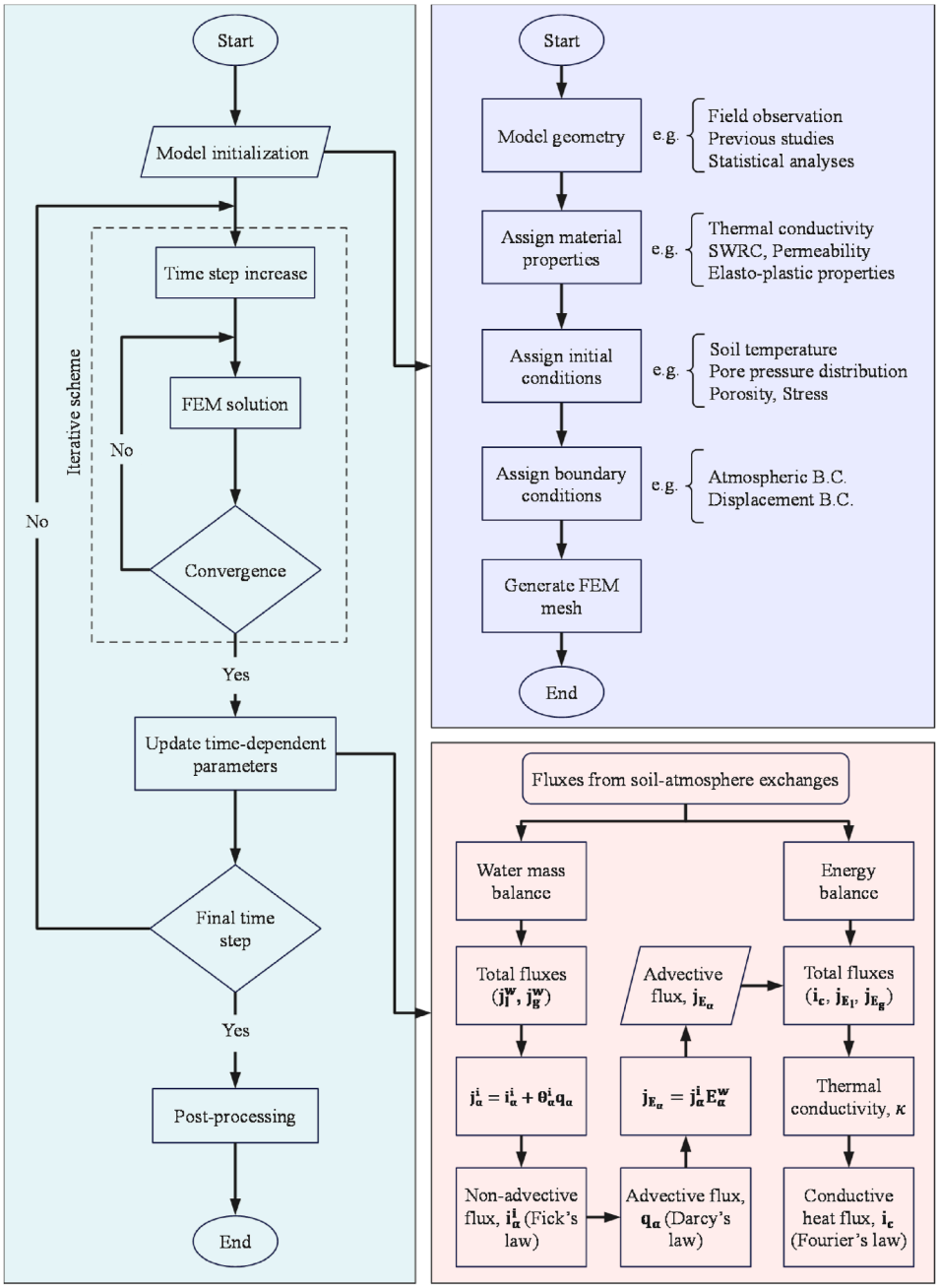

Fig. 7. Flowchart of the numerical model derivation and fundamental processes.

d rainfall), 182 (with a temperature of 39.1 °C), and 567 (with a temperature of 38.9 °C) is shown in Fig. 9. As observed in Fig. 9a, micro-porosity at the edges of the crack reaches its highest value at 0.234, indicating a 30% increase in the volume of microstructure pores. Additionally, due to water infiltration through the soil surface and crack walls, these areas also experience an increase in micropore volume due to swelling, with the most significant swelling occurring at the crack edges. This heterogeneous distribution of pore volume changes can lead to differential soil surface deformation due to the presence of cracks, potentially endangering structures on the ground. On warmer days of the year, such as the 182nd and 567th days of the first and second years respectively, surface desiccation occurs both from the soil surface and crack walls, with maximum shrinkage similarly occurring at the crack edges. The results indicate that a depth of about 25 cm from the ground surface and crack tip is affected by climatic changes, while the remaining soil areas maintain the initial micro-porosity value of 0.18.

The volumetric changes in cracked soil during wetting and drying cycles occur elasto-plastically. In the elastic region, deformations are reversible, while upon entering the plastic region, deformations become irreversible, and plastic strain is induced in the soil. Fig. 10 illustrates the changes in volumetric plastic strain between the 3rd and 4th cracks as a function of suction and time. According to the results in Fig. 10a, the volumetric plastic strain increases annually. Quantitatively, the maximum plastic strain in the first year is 16.8%, in the second year is 18.1%, and in the third year is 19.7%. These values indicate nonlinear changes in plastic

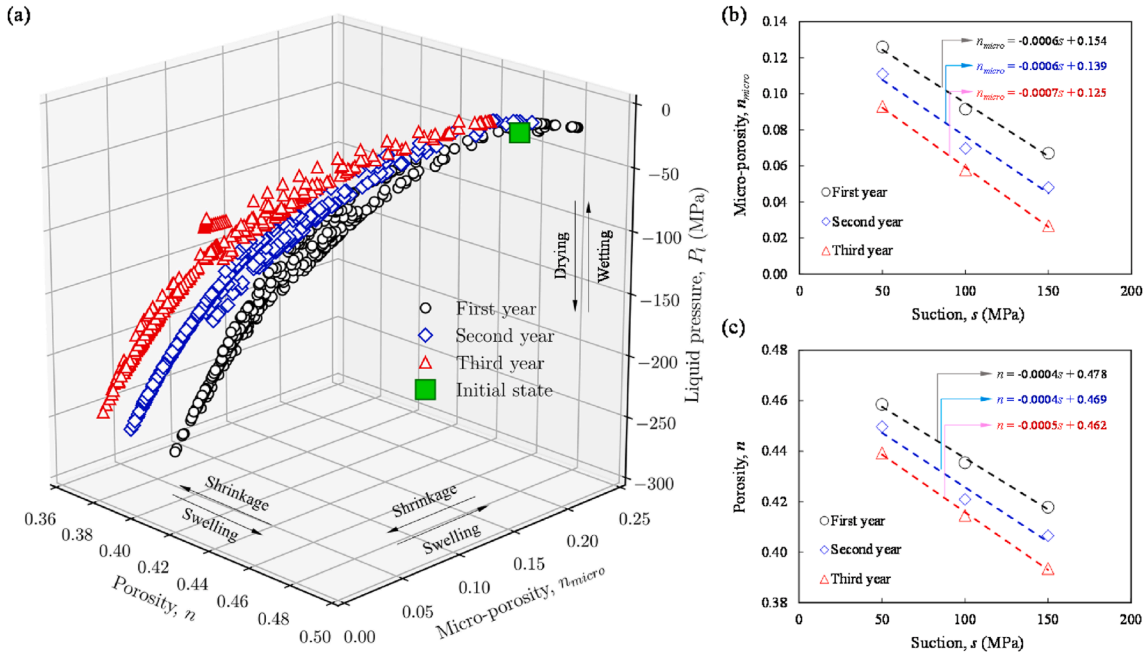

Fig. 8. (a) 3D view of simultaneous variations in porosity, micro-porosity, and liquid pressure, (b) selective representation of variations in micro-porosity with suction, and (c) selective representation of variations in porosity with suction.

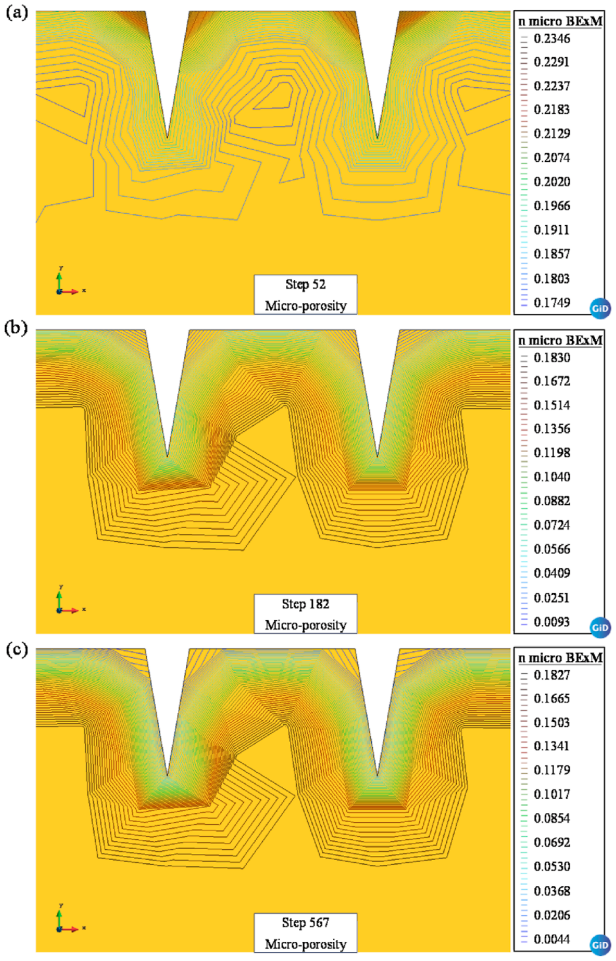

Fig. 9. 2D distribution of micro-porosity near 3rd and 4th cracks after (a) 52 d, (b) 182 d, and (c) 567 d.

strain, which eventually reach equilibrium after experiencing various thermo-hydraulic cycles, resulting in a reduced rate of changes.

By fixing the product of pore water pressure and porosity (nP_l) at values of −20, −50, and −80 MPa, the plastic strain as a function of time is shown in Fig. 10b. Interestingly, plastic strain depends on both time and nP_l. Over time and through different natural seasons, plastic strain continues to increase. Moreover, as nP_l increases, the plastic strain also increases, and its changes occur with a steeper gradient. Quantitatively, with a fourfold increase in nP_l from −20 to −80, the gradient of plastic strain changes by a factor of 2.3. The variations in plastic strain along with porosity over three years were presented in Fig. 10c. This result shows that these changes form a linear pattern over three years, following the relationship below, indicating an increase in plastic strain with a decrease in porosity due to desiccation:

$$\varepsilon_{vp} = -167.19n + 82.3 \tag{31}$$

The variations in swelling pressure along with volumetric plastic strain during wetting-drying cycles are indicated in Fig. 11. When soil dries, the water within the soil pores evaporates, causing the soil particles to draw closer together. This reduction in volume results in negative swelling pressure. The negative values of swelling pressure observed in the results indicate that the soil is experiencing a shrinking force, which is common during drying paths. This force opposes the expansion caused by wetting and is a critical factor in the soil's volumetric behavior during alternating wetting and drying periods. In other words, the negative swelling pressure is a measure of the soil's resistance to volume increase during drying. Moreover, the soil's elasto-plastic behavior under cyclic wetting and drying conditions means that each drying cycle leads to an incremental increase in plastic strain and corresponding negative swelling pressure. This accumulation of plastic strain over time is indicative of the soil's adaptation to the environmental conditions, where it undergoes irreversible changes that manifest as negative swelling pressure.

Irreversible volumetric changes resulting from wetting-drying

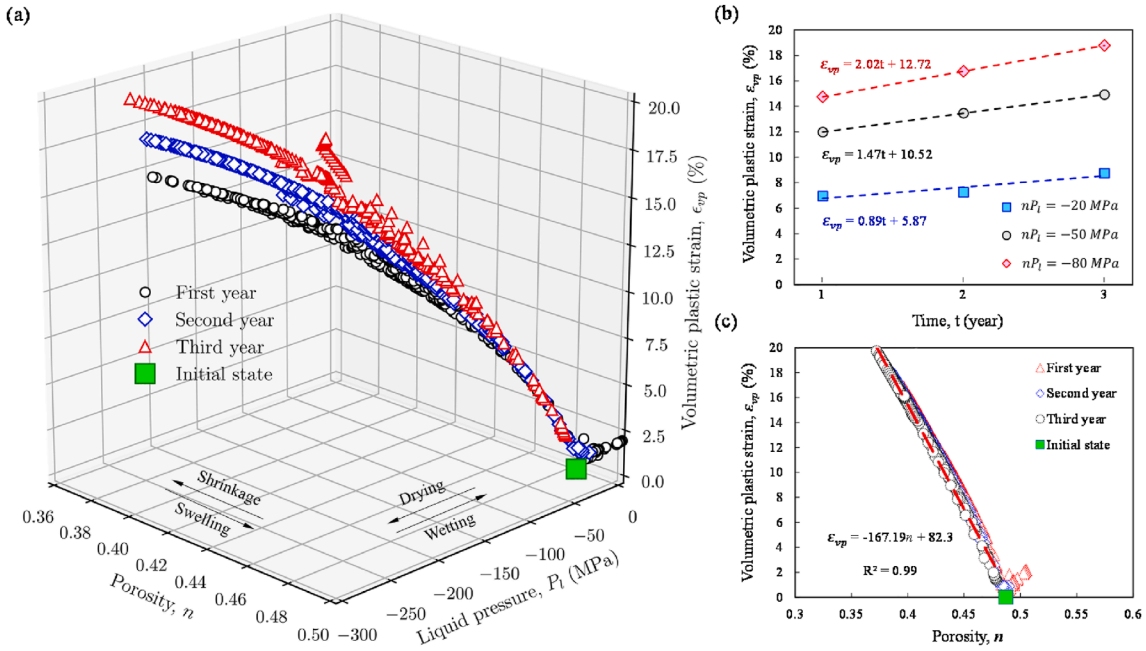

Fig. 10. (a) 3D view of simultaneous variations in porosity, liquid pressure, and volumetric plastic strain; (b) Selective representation of variations in volumetric plastic strain with time; and (c) Selective representation of variations in volumetric plastic strain with porosity.

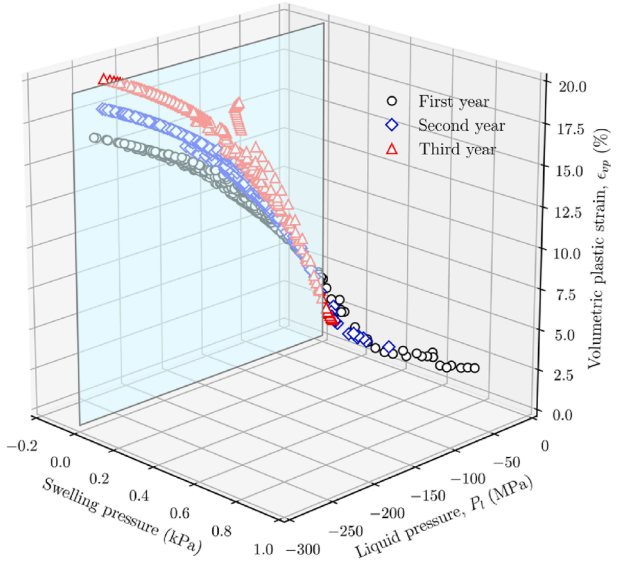

Fig. 11. Dependency of volumetric plastic strain on swelling and liquid pressures.

cycles are critical for understanding the long-term stability of soils in various geotechnical applications. These changes, primarily caused by cyclic swelling and shrinkage, accumulate over time and significantly affect soil behavior, particularly in expansive clays. Studies indicate that desiccation cracks alter the soil's structural integrity, influencing stress redistribution, porosity, and water flow paths. The presence of cracks amplifies deformation mechanisms. For instance, during wetting, cracks serve as preferential water infiltration paths, accelerating soil saturation and reducing suction. This rapid reduction in suction increases the mobility of soil particles, leading to localized shear and volumetric strains along crack edges. Over time, these irreversible strains manifest as cumulative settlement, differential deformation, and potentially instability in slopes, retaining walls, and embankments.

The laboratory experiments highlighted that both macro- and microcracks contribute to these deformations, reducing the soil's ability to recover its original state after each cycle (Tang et al., 2023). In addition to settlement and deformation, the accumulation of irreversible strains has implications for geohazards such as landslides and subsidence in expansive soils (Sadeghi et al., 2024). The crack-induced heterogeneity in soil stiffness and strength alters the stress distribution, creating weak zones susceptible to failure under additional loading, such as heavy rainfall or seismic events. Furthermore, as evidenced in studies on unsaturated soils, cyclic temperature and suction variations exacerbate these effects, particularly in regions experiencing climate extremes (Zhou and Ng, 2016).

From an engineering perspective, incorporating these irreversible volumetric changes into design methodologies is essential. For example, in foundation engineering, crack-induced settlement must be considered in serviceability limit state calculations to ensure structural safety over time. Similarly, for pavement design, accumulated plastic strains from cyclic loading, coupled with climate-induced suction variations, should inform maintenance schedules and material selection. In slope stability analysis, crack propagation and water infiltration must be explicitly modeled to evaluate the likelihood of failure under dynamic climatic conditions.

5.2. Spatio-temporal redistribution of stress

The 2D distribution of vertical, horizontal, and shear stresses on the 52nd day (coinciding with the first wetting path) and the 182nd day (coinciding with the warmest day over three years with a temperature of 39.1 °C) is compared in Fig. 12. As a general rule in this study, compressive stresses and shrinkage strains are denoted by negative values, while tensile stresses and swelling strains are indicated by positive values. As is evident from Fig. 12a after a rainfall, the compressive horizontal stress (σ_x) at the crack tip showed a concentration of approximately −0.004 kPa. The

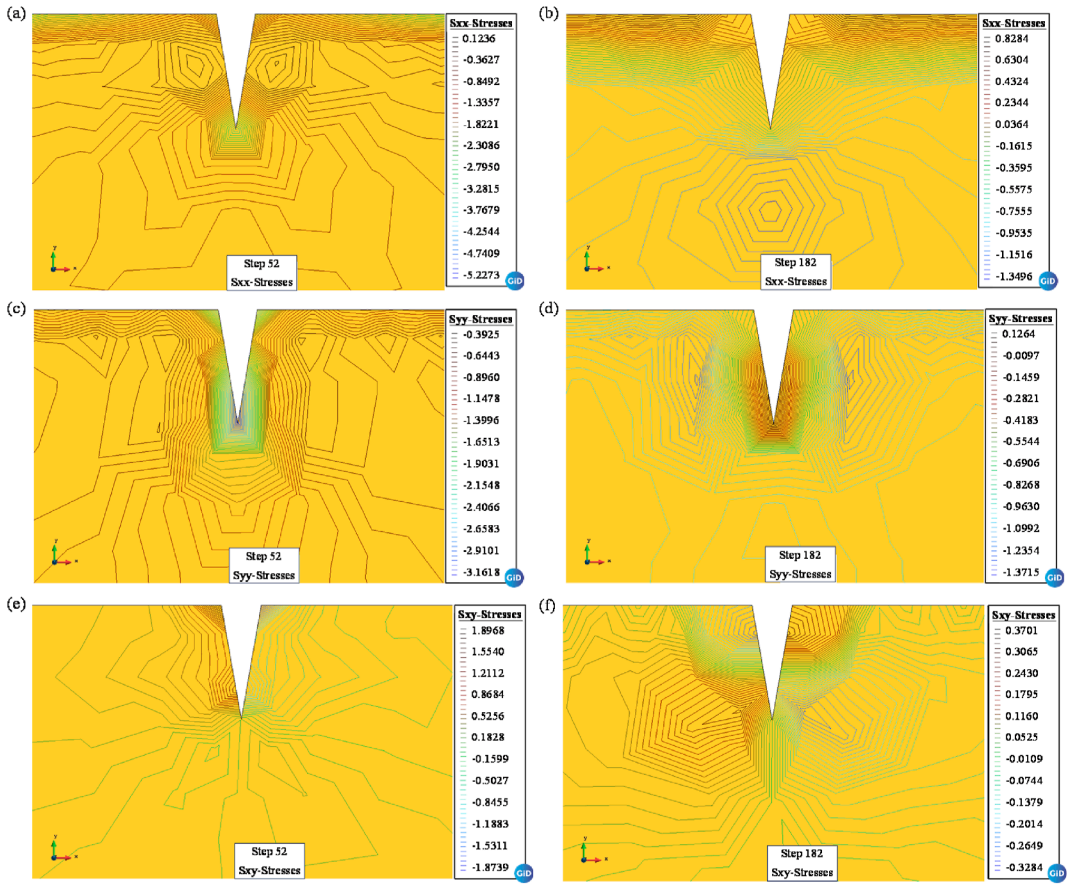

Fig. 12. 2D stress redistribution near 9th crack (kPa): (a) σ_x on day 52, (b) σ_x on day 182, (c) σ_y on day 52, (d) σ_y on day 182, (e) τ_{xy} on day 52, and (f) τ_{xy} on day 182.

negative horizontal stress at the crack tip indicates compressive forces, which are likely due to the soil swelling upon wetting. The localized increase in horizontal stress at the crack tip can be attributed to the rapid water infiltration and subsequent soil expansion, causing compression in the horizontal direction.

During warm days, the surface of the soil exhibited positive horizontal stress values of 0.0008 kPa, as shown in Fig. 12b. The positive horizontal stress at the surface indicates tensile forces, which can be attributed to the desiccation and shrinkage of the soil due to high temperatures. As depth increased, the horizontal stress transitioned to negative values, reaching −0.0013 kPa below the crack tip. The negative horizontal stress observed at deeper levels below the crack tip suggests compressive forces, likely due to the overburden pressure and the relative immobility of deeper soil layers compared to the surface.

The vertical stress (σ_y) distribution indicates a compressive stress concentration at the crack walls and tip, with values ranging from −0.002 to −0.003 kPa after rainfall, as shown in Fig. 12c. This compressive stress is attributed to the initial wetting of the soil, causing it to swell and exert pressure on the crack boundaries. The compressive stress decreases radially from the crack tip, indicating the localized nature of the swelling-induced stress. The stress dissipates moving away from the crack, reducing in magnitude but still indicating a zone of influence. On the 182nd day, the vertical stress (Fig. 12d) shows a similar stress pattern at the crack walls and tip, however, distinct mechanism with tensile stresses around 0.0001 kPa. The stress distribution extends further from the crack tip compared to the 52nd day, suggesting an ongoing stress adjustment due to prolonged environmental exposure. This indicates that the crack tip is the area most susceptible to further propagation.

The shear stress (τ_{xy}) distribution near the 9th crack reveals a symmetrical pattern along the crack walls after a rainfall, as shown in Fig. 12e. This suggests that the direction of deformation or movement on the two opposing crack boundaries is in opposite directions. In the context of shear stresses, the positive and negative values do not represent tension or compression as in the case of normal stresses. Instead, they indicate the direction of the shear forces acting on a plane, relative to a chosen coordinate system. When defining shear stresses in a Cartesian coordinate system where the positive y-axis is upward and the positive x-axis is rightward, the sign of shear stress depends on the direction of the force acting on the soil element faces. Positive shear stress ($+\tau_{xy}$) occurs when the force on the rightward face is directed upward and the force on the upward face is directed rightward, causing clockwise rotation of the soil element. Negative shear stress ($-\tau_{xy}$) occurs when the force on the rightward face is directed downward and the force on the upward face is directed leftward, causing counterclockwise rotation.

For example, during the wetting path (Fig. 12e), the soil swells, and the crack width decreases. This is reflected in the shear stress distribution, where the right crack edge exhibits negative shear stress, and the left crack edge shows positive shear stress. By examining the deformed state of soil elements along the crack edges, it can be inferred that the opposing edges of the crack move toward each other, leading to crack closure. On the other hand, during the drying path (Fig. 12f), the soil shrinks, causing an increase in crack width. The right crack edge experiences positive

shear stress, while the left crack edge undergoes negative shear stress, reversing the deformation behavior seen in the wetting path. On the 182nd day, the shear stress redistribution pattern changes significantly. Specifically, shear stress decreases with the shrinkage of the soil. Simultaneously, negative shear stress is observed at the left head of the crack, while positive shear stress is observed at the right head. Along the crack walls, the sign of the shear stress alternates, with notable shear stress localization at the crack tip. Overall, a wedge-like formation, similar to a failure wedge, develops in the crack region, indicating concentrated and localized shear stresses in the crack areas under climatic changes. This emphasizes the shear crack mechanism; however, it is negligible with respect to the tensile crack mechanism.

The predominance of the tensile crack mechanism over the shear crack mechanism is supported by several observations. First, cracks primarily initiate and propagate due to tensile stresses, which exceed the soil's tensile strength during desiccation. Second, the magnitude of tensile stresses is significantly greater than that of localized shear stresses, as shown in Fig. 12e and f. Third, while shear stresses are confined to regions near crack tips and walls, tensile stresses have a broader spatial influence, driving crack widening and propagation. Consequently, shear stresses play a secondary role in localized deformation, whereas tensile stresses govern the overall cracking process. It is therefore interesting that the role of shear stress was also revealed in this study, although the role seems to be relatively marginal compared to the tensile stress.

The results can be further supported by the principles of fracture mechanics, which provide a robust framework for understanding crack initiation and propagation. Cracks in materials occur in three primary modes: Mode I (opening mode), Mode II (sliding mode), and Mode III (tearing mode). In Mode I, crack faces displace perpendicular to the crack plane due to tensile stresses. In Mode II, crack faces slide over each other parallel to the crack front due to in-plane shear stresses. In Mode III, crack faces slide relative to each other parallel to the crack front due to out-of-plane shear stresses. The stress intensity factors (SIFs) are critical parameters in fracture mechanics, describing the stress state near the crack tip for each mode. For Modes I and II, the SIFs can be expressed by the following simplified equations (Knott, 1973):

$$\left.\begin{aligned} K_{\mathrm{I}} &= \sigma\sqrt{\pi a} \\ K_{\mathrm{II}} &= \tau\sqrt{\pi a} \end{aligned}\right\} \tag{32}$$

where K_{I} and K_{II} are the SIFs for Modes I and II, respectively; a is half of the crack length; and σ and τ are the normal and shear stresses, respectively. A crack propagates when the SIF exceeds the material's fracture toughness ($K \geq K_{\mathrm{C}}$), which is the critical SIF beyond which the material can no longer resist crack growth. Additionally, the energy release rate (G) is another fracture criterion that evaluates cracking from an energy perspective and refers to the energy released when a crack expands per unit area (Xu et al., 2022). For Modes I and II, the energy release rates under plane strain conditions are given by

$$\left.\begin{aligned} G_{\mathrm{I}} &= \frac{1-\nu^2}{E}K_{\mathrm{I}}^2 \\ G_{\mathrm{II}} &= \frac{1-\nu^2}{E}K_{\mathrm{II}}^2 \end{aligned}\right\} \tag{33}$$

where E is the elastic modulus and ν is the Poisson's ratio. A crack propagates when $G \geq G_{\mathrm{C}}$, where G_{C} is the critical energy release rate. These criteria highlight the interplay between stress intensity, energy dissipation, and material resistance in controlling crack propagation. In the context of this study, the fixed crack depth assumption simplifies the analysis by focusing on stress redistribution patterns. Based on the results presented in Fig. 12b–d, and f, extreme drying conditions induced by arid climates lead to significant stress localization near cracks. The horizontal normal stress localizes primarily on the soil surface, particularly in tensile zones where drying-induced shrinkage occurs. This increases the SIF (K_{I}) and energy release rate (G_{I}), potentially exceeding the threshold values (K_{C}, G_{C}) required for crack propagation (Fig. 12b). The vertical normal stress and shear stress concentrates along crack walls and at crack tips, consistent with stress redistribution patterns under multi-physical conditions (Fig. 12d and f). These localized stresses elevate K_{I} and G_{I} for vertical stress and K_{II} and G_{II} for shear stress, suggesting a high potential for Mode II and mixed-mode cracking near the crack walls and tip.

The fracture mechanics principles imply that the crack tip is the most vulnerable zone for further propagation or branching, particularly under mixed-mode conditions where both tensile and shear stresses act concurrently. In expansive soils, cracks form and propagate due to the interplay of matric suction, environmental loading, and soil strength. Drying cycles increase suction, leading to tensile stress accumulation and Mode I cracking, while wetting cycles reduce suction but may promote shear displacement along existing cracks (Mode II). The coupling of hydraulic and mechanical fields intensifies stress redistribution, with crack networks evolving to balance the soil's energy state.

For a surface crack in a semi-infinite medium (i.e. a crack on the soil surface extending downward), the Mode I stress intensity factor can be estimated as

$$K_{\mathrm{I}} = Y\sigma\sqrt{\pi a} \tag{34}$$

where Y is the geometry correction factor that depends on crack shape, depth, and boundary conditions. For a long, surface-breaking crack in a semi-infinite domain, a common approximation for drying-induced shrinkage stress is

$$K_{\mathrm{I}} = 1.12\sigma\sqrt{\pi a} \tag{35}$$

Parameter a in soil as a semi-infinite medium with surface desiccation cracks is considered to be the crack depth. Since Mode I SIF characterizes desiccation-induced cracking, the minimum principal stress (σ_i) is used in the calculation of K_{I}. This assumption aligns with the study by Houcem et al. (2023), which also considered the minimum principal stress as the primary tensile stress driving soil crack propagation.

To analyze the spatial and temporal variations in K_{I} under wetting and drying cycles, specific time periods were selected, capturing both rainfall events and high-temperature conditions. The two-week period from day 41 to day 54 was chosen to examine rainfall effects due to significant precipitation during this time, while the time span of day 175 to day 188 was selected to evaluate the impact of high temperatures on soil drying and fracture behavior. To investigate spatial variations in K_{I}, three distinct locations along the crack were examined: crack tip where stress concentration is the highest and crack propagation is most likely, crack edge located at the soil surface and is influenced by direct atmospheric boundary effects, and middle of the crack wall representing stress conditions within the crack itself.

The variations in K_{I} under wetting and drying paths are illustrated in Fig. 13. As shown in Fig. 13a, during the wetting path, rainfall infiltration reduces tensile stress due to soil swelling and stress relaxation, leading to a decrease in K_{I}. The results indicate that K_{I} drops as low as -3.9 kPa $\mathrm{m}^{1/2}$ during periods of high rainfall, while in the absence of precipitation, K_{I} increases to 1.2 kPa $\mathrm{m}^{1/2}$. A positive K_{I} indicates that the crack tip experiences

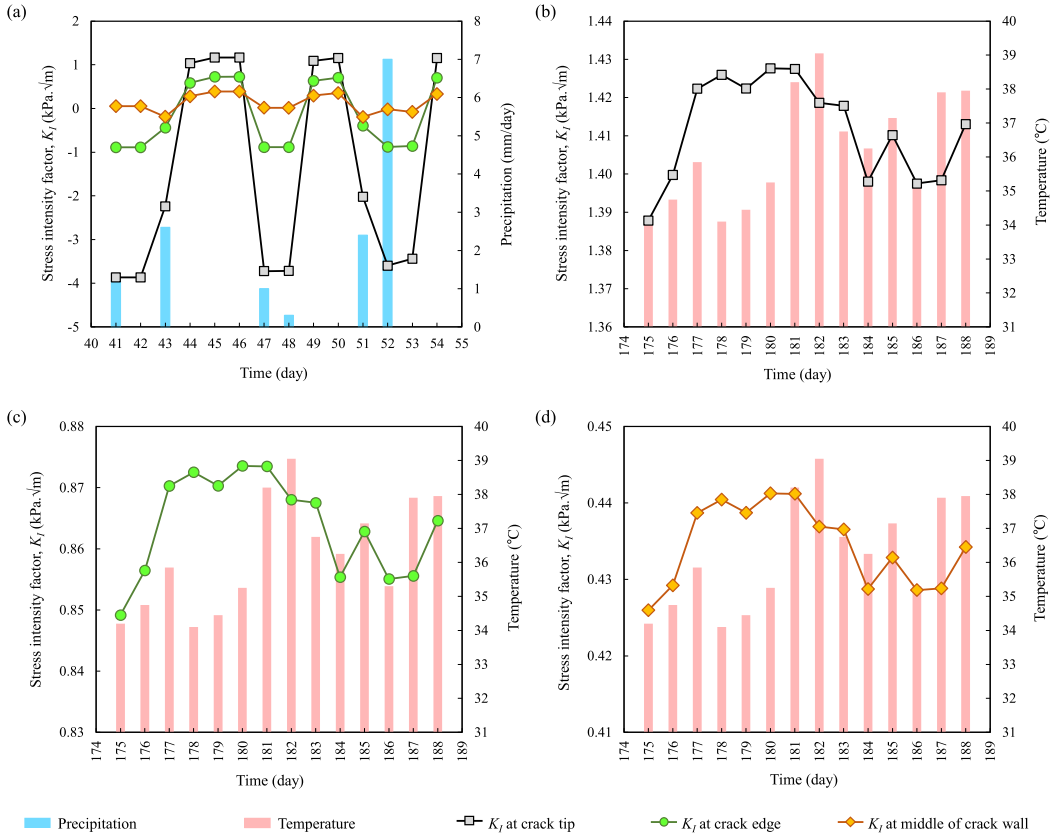

Fig. 13. Spatio-temporal variations of Mode I stress intensity factor (K_I) under (a) rainfall and (b–d) high temperatures at three crack locations, including the crack tip, crack edge, and the middle of the crack wall.

tensile opening if $K_I > K_C$. A negative K_I suggests that the crack is subjected to compressive stress, which tends to close the crack rather than to promote its growth. The findings reveal that the crack tip experiences the most significant fluctuations, emphasizing its role as the primary location for potential crack propagation. The crack edge shows moderate fluctuations, with K_I ranging between −1 and +1 kPa $m^{1/2}$. The middle of the crack wall exhibits the lowest variations between −0.2 and 0.4 kPa $m^{1/2}$, suggesting a relatively stable stress distribution within the crack compared to its extremities.

In contrast, as soil dries under high temperatures, desiccation-induced shrinkage increases tensile stress, leading to a rise in K_I. The results show that at the crack tip, K_I increases from 1.39 kPa $m^{1/2}$ to 1.43 kPa $m^{1/2}$, suggesting a higher probability of crack propagation under severe drying conditions. The highest K_I values are consistently observed at the crack tip, confirming that cracks are most likely to propagate from the tip rather than initiate new fractures along the crack wall. This observation is consistent with classical fracture mechanics, where the tip acts as a stress concentrator, accumulating sufficient energy for crack extension.

Based on the calculation of K_I, the energy release rate can also be determined. Eq. (33) presents a straightforward relationship between the Mode I stress intensity factor and the energy release rate. Although this equation applies to materials exhibiting linear elastic behavior, it is utilized here to provide additional insights from a simplified perspective. The elastic properties of Boom clay, the soil material examined in this study, have been extensively documented in previous research. The Young's modulus of Boom clay has been reported to range from 100 MPa to 400 MPa, with a Poisson's ratio of approximately 0.4. According to the study of Dehandschutter et al. (2005), Young's modulus and Poisson's ratio are assumed to be 200 MPa and 0.4, respectively.

Fig. 14 illustrates the spatio-temporal variations of G_I under rainfall and high temperatures at the crack tip, crack edge, and middle of the crack wall. The energy release rate represents the amount of energy available for crack propagation per unit of newly created fracture surface. Under extreme climatic conditions, the energy release rate G_I tends to be high. Since G_I depends on K_I^2, it always yields a positive value, indicating that it does not differentiate between compressive and tensile stress states. As shown in Fig. 14a, although the energy release rate at the crack tip is high in rainfall conditions, the dominant stress mode is compressive. A comparison of Fig. 14a–c reveals that, similar to K_I, the most significant fluctuations in G_I up to 63 mJ/m^2 occur at the crack tip, while moderate changes are observed at the crack edge, and the least variations are found at the middle of the crack wall.

High G_I during drying conditions corresponds to tensile stress at the crack tip, which directly contributes to crack propagation. This leads to progressive soil degradation, exacerbating desiccation cracking over time. Fig. 14d illustrates that at elevated temperatures of approximately 39 °C, G_I reaches 8.6 mJ/m^2 at the crack tip, 3.2 mJ/m^2 at the crack edge, and 0.82 mJ/m^2 at the midpoint of the crack wall. Based on these analyses, in soil with pre-existing cracks, the crack tip is the most vulnerable zone for fracture growth due to stress concentration and the available energy for release. Additionally, the crack edge, or the soil surface in general, is particularly susceptible to desiccation cracking because of direct exposure to environmental loading, making it prone to enhanced degradation.

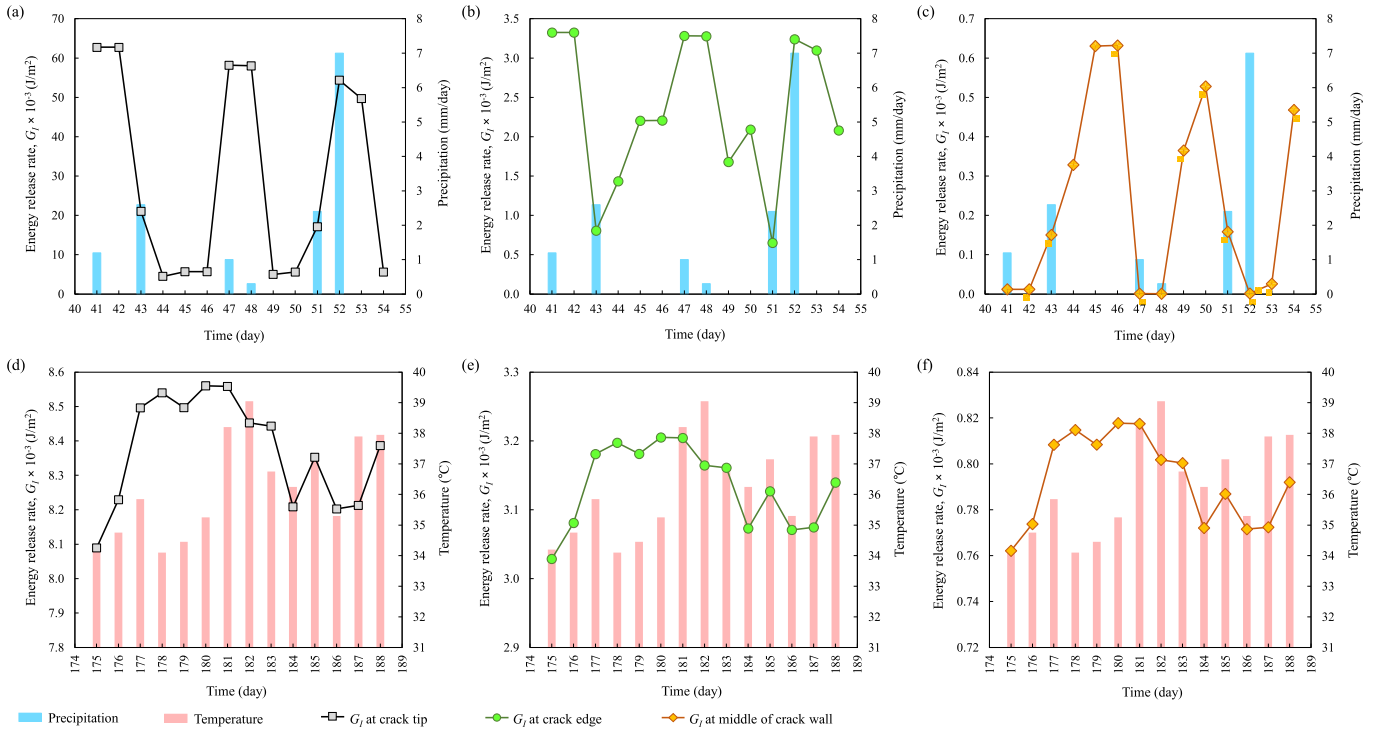

Fig. 14. Spatio-temporal variations of Mode I energy release rate (G_I) under (a–c) rainfall and (d–f) high temperatures at three crack locations, including the crack tip, crack edge, and the middle of the crack wall.

Arid regions often experience extreme temperature fluctuations and low moisture levels, which can lead to significant soil shrinkage and cracking. Therefore, for investigating the potential crack initiation and propagation, it is useful to utilize principal stresses which are showing the minimum and maximum stresses experienced by the soil. Fig. 15a illustrates the variations in minimum principal stress (σ_i) in relation to changes in pore volume and pore water pressure. Based on the boundary surface plotted at zero principal stress, it is observed that as the soil undergoes successive wetting and drying cycles over several years, the minimum principal stress shifts from compression to tension. Due to the limitations of the finite element method, the occurrence of new cracks in addition to existing ones cannot be directly observed. However, considering the shrinkage crack mechanism resulting from tensile stresses, it is inferred that desiccation cracking is likely to occur. This behavior is strongly dependent on the studied climate and soil properties. Fig. 15b displays the maximum principal stress (σ_{iii}), indicating a decrease in compressive stress over the three-year period. Insights from Fig. 15 indicate that during the drying process, the soil surface experiences significant tensile stresses as a direct result of shrinkage caused by water evaporation. As moisture is lost from the soil pores, the internal suction increases, leading to a reduction in volume. This phenomenon highlights the critical role of tensile stress in the drying process, as the soil must accommodate the changes in moisture content while maintaining structural integrity. Furthermore, the analysis reveals that successive wetting-drying cycles contribute to a gradual reduction in compressive stresses within the soil matrix. With each cycle, the compressive forces that initially act to stabilize the soil diminish, creating an environment where tensile stresses become increasingly dominant. Over time, this transition results in a pronounced shift toward tensile-dominated behavior, particularly evident in the later stages of the drying process.

Fig. 16 illustrates the 2D distribution of principal stresses around the 3rd and 4th cracks for days 52 (after rainfall) and 182 (the warmest day). According to Fig. 16a, the increase in pore water pressure during the wetting path induces compressive stresses in the minimum principal stress at the soil surface between the two cracks and at the crack tips, which occurs due to soil swelling. Fig. 16c on the same day shows the 2D distribution of maximum principal stress, where compressive stress concentration is seen along the crack edges. During the drying paths, the minimum principal stress, as shown in Fig. 16b, demonstrates that tensile stresses intensify at the soil surface, crack walls, and crack tips. This is due to the increased suction that occurs during soil drying, leading to soil shrinkage. In deeper regions of the cracks, compressive stresses prevail. Additionally, the maximum principal stress during the drying paths shows a significant decrease along the crack walls and tips, as seen in Fig. 16d, indicating that the soil transitions from a compressive to a tensile stress state near the cracks.

6. Discussion

6.1. Mutual dependence of stress, strain, and pore water pressure

This study corroborates previous research that has emphasized tensile stress as a primary driver of soil cracking. However, it also highlights the significant role of shear stress, which, although less dominant, cannot be ignored in the comprehensive analysis of soil cracking mechanisms. The insights gained from the 2D stress distributions around cracks provide valuable information on the localized stress concentrations and their implications for soil deformation. The observed stress patterns indicate that crack tip is the most critical area where stress concentration is most pronounced, making them susceptible to further crack propagation. According to Fig. 12a, during the rainfall and infiltration process,

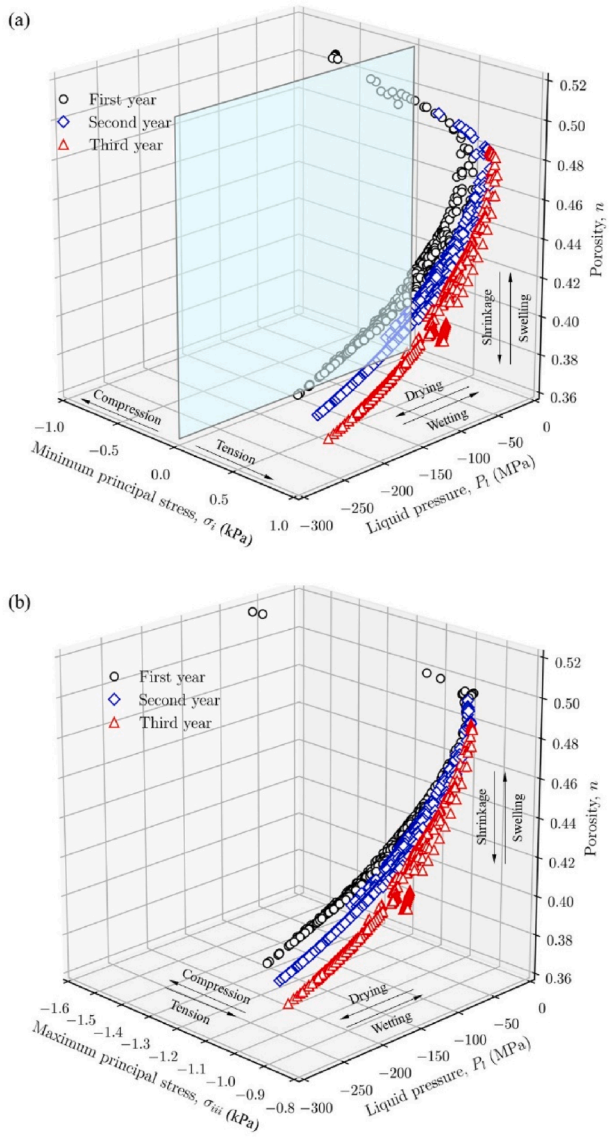

Fig. 15. Variations in (a) minimum and (b) maximum principal stresses with liquid pressure and porosity.

the crack tip experiences the highest compressive horizontal stress. Specifically, during the wetting phase, the horizontal stress at the crack tip increases by 5.22 times its initial value. Comparing this result with Fig. 16c, it can be observed that the maximum principal stress is 7.55 times the initial compressive stress at the crack edges. Therefore, while the crack tip endures maximum horizontal stress due to crack closure during soil swelling, the crack edges face the most severe compressive principal stress, indicating critical swelling at these edges. This conclusion is supported by Fig. 9a, which shows a significant increase in micro-porosity at the crack edges during rainfall, with a 30% rise in micro-porosity in this critical area.

Moreover, the observed results in Fig. 12e and f indicate that in cracked soil, shear stress increases with rising soil moisture due to rainfall, and decreases with soil drying. This relationship between soil moisture and shear stress can be linked to the shear cracking mechanism. During rainfall, soil moisture increases as water infiltrates the soil, reducing soil suction. The reduction in suction leads to soil particles becoming more lubricated, less tightly bound, and the water molecules start to separate the clay particles, reducing the attractive forces between them. This increased lubrication and particle separation allows the soil to deform more easily under applied stresses, resulting in higher shear stress concentrations. In cracked soil, these increased shear stresses are especially pronounced along the crack edges and tips where water infiltration is highest. The higher shear stress during wetting can facilitate the mobilization of soil particles along the crack surfaces, potentially leading to shear displacement or even further crack propagation if the shear stress exceeds the soil's shear strength. In addition, this phenomenon can manifest differently in deep and wide cracks. Due to increased shear stress, the upper edges of the crack can fail, leading to crack widening along the wetting path through a shear failure mechanism. Shear cracks typically form parallel to the direction of the shear stress. Therefore, based on the contour lines presented in Fig. 12e, this shear failure at the crack edges can be anticipated. This widening leads to the expansion of the space inside the crack, which in turn intensifies evaporation and infiltration processes. Consequently, these dynamics contribute to the gradual enlargement of the crack over time.

Conversely, during drying periods, soil moisture decreases and suction increases. The increased suction causes soil particles to be drawn closer together, increasing interparticle friction and cohesion. This increased cohesion restricts the soil's ability to deform, resulting in lower shear stress. As the soil dries, it becomes more rigid and less prone to shear displacement, which decreases the likelihood of shear-induced crack propagation. However, the increased rigidity can lead to higher tensile stresses, which are more likely to cause tensile cracking.

In the previous sections, the stress and strain evolutions were separated to be elucidated distinctly. However, their variations are simultaneous and should be considered at the same time. In this context, Fig. 17 illustrates the simultaneous changes in vertical stress (σ_y), vertical strain (ε_y), and pore water pressure (P_l) over a period of three years between 3rd and 4th cracks. According to Fig. 17a, the initial conditions include compressive stress values of 1 kPa, zero strain, and pore water pressure of −10 MPa. In the initial days of the first year, limited positive vertical strains, indicating soil swelling, are observed due to rainfall. This is because the soil, in its initial state, has not yet experienced any hydraulic paths and shows more swelling behavior in response to an initial wetting path. However, after undergoing several wetting and drying cycles, the swelling potential decreases, and the strains predominantly fall within the range of 5%–10% shrinkage strains.

The dependency between stress-strain and stress-suction was separately shown over these three years in Fig. 17b and c. As observed, with the decrease in soil moisture content due to the arid climate, the suction in the soil increases. The increased suction leads to a shift in stress towards lower compressive stresses, corresponding to the mechanism of shrinkage cracks induced by tensile stresses.

The simultaneous variations in vertical stress, liquid pressure, and porosity separated with annual variations in Fig. 18. During the first year, the soil undergoes its initial cycles of wetting and drying. As drying occurs, suction increases, leading to a reduction in porosity due to soil shrinkage. This shrinkage is accompanied by a decrease in compressive vertical stress, moving the stress state towards tensile stress. In the second year, the trend observed in the first year persists, but with more pronounced shifts. The cyclic variations become more evident as the soil undergoes further

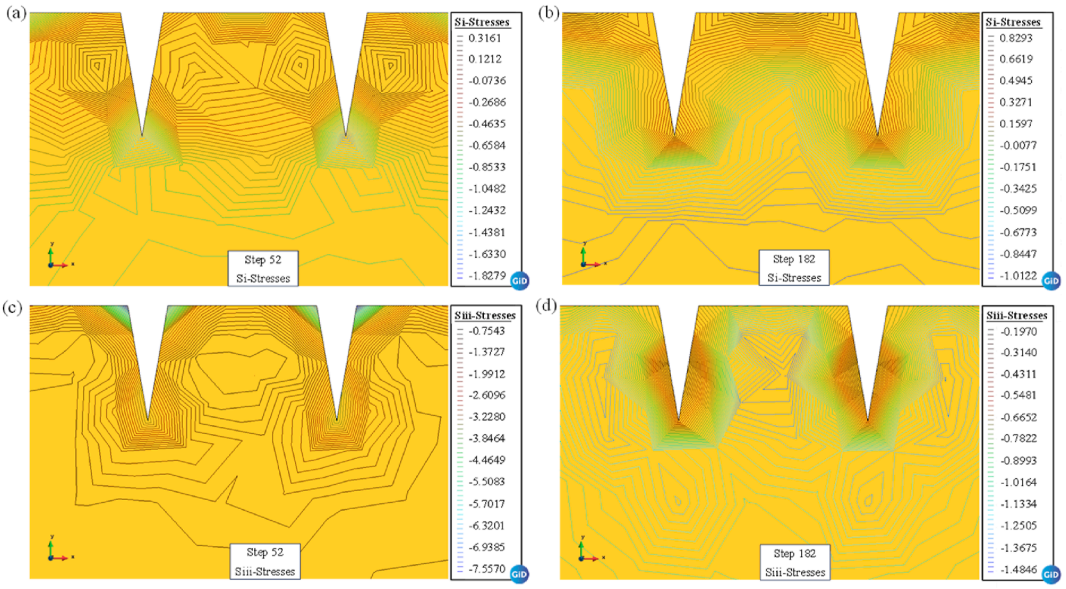

Fig. 16. 2D principal stress redistribution (kPa) around 3rd and 4th cracks: (a) Minimum stress on day 52, (b) Minimum stress on day 182, (c) Maximum stress on day 52, and (d) Maximum stress on day 182.

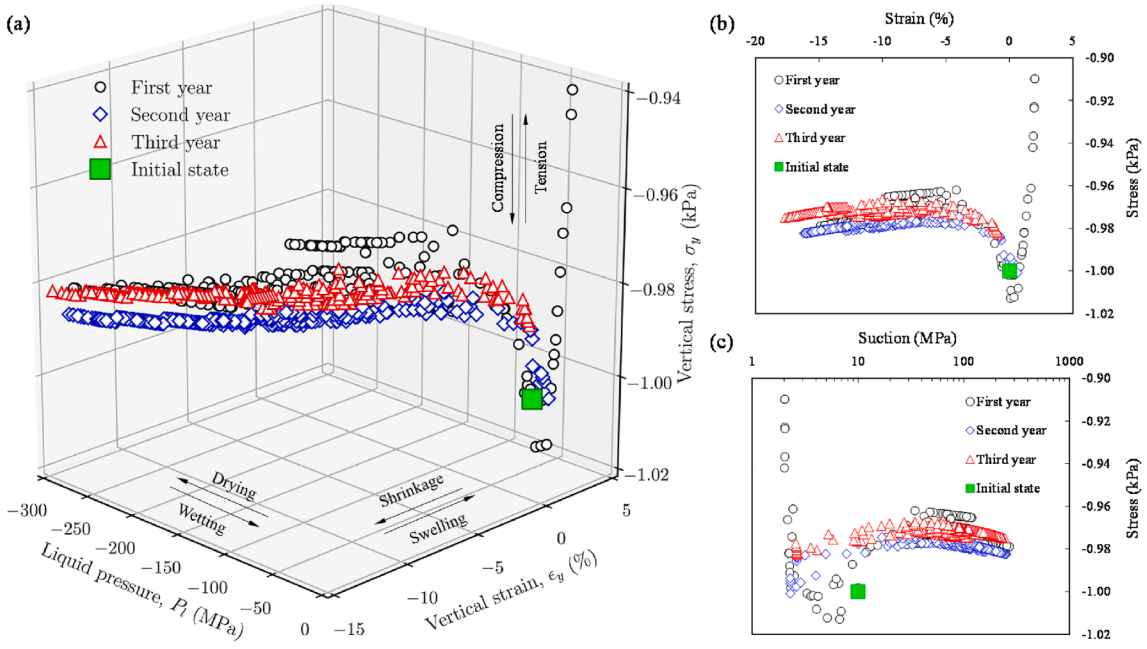

Fig. 17. (a) Simultaneous variations in vertical stress, vertical strain, and liquid pressure in 3D view and separate dependence of vertical stress on (b) vertical strain and (c) suction.

shrinkage and desiccation, reducing porosity and shifting the vertical stress further towards tensile stress. The movement in the plot indicates that the soil is adapting to the repetitive cycles, with the stress state trending more consistently towards tensile regions. By the third year, the soil has undergone multiple wetting-drying cycles, leading to significant desiccation. The plot shows an even further shift towards the right along the vertical stress axis, indicating increased tensile stress. The porosity continues to decrease, reflecting substantial shrinkage. The results also indicate the severe reduction in void volumes during soil shrinkage. Since the studied area has an arid climate, soil tends to shrink rather than swell. Therefore, the reduction of 22% can be concluded from the porosity variations during three-year period.

6.2. Model applicability and future research directions

The real-world data used in this study, including meteorological inputs (e.g. temperature, precipitation, and radiation) from Qom, Iran, and the parameters for Boom clay, were selected because they represent realistic environmental conditions and well-studied soil properties. These parameters were incorporated into the model calibration and validation processes to capture the

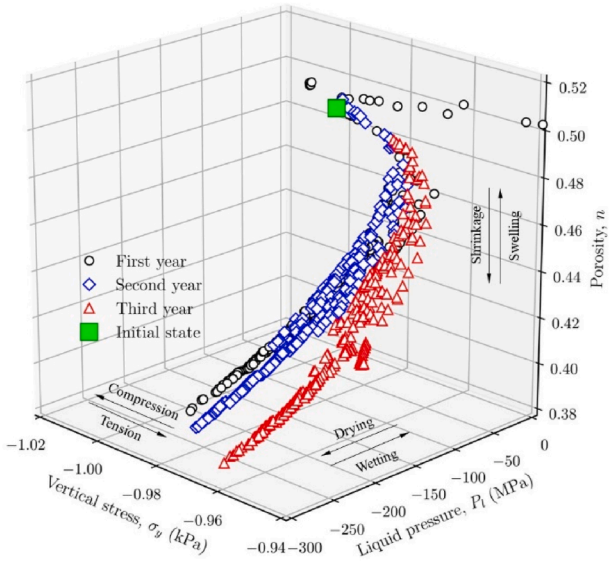

Fig. 18. 3D view of simultaneous variations in vertical stress, liquid pressure, and porosity.

essential physical phenomena driving the thermo-hydro-mechanical behavior of desiccation-cracked soils. The parameters utilized in this study reflect specific conditions, including a semi-arid climate, deep water table, thick vadose zone, low annual rainfall, and particular soil characteristics. However, the governing equations and constitutive relationships employed in the model are applicable in a broader context. Therefore, the model can be applied to other climates and soil types by adjusting input parameters, such as soil hydraulic properties, thermal conductivity, and mechanical behavior, to match site-specific conditions. The findings demonstrate that the model is robust and generalizable, making it applicable to a range of semi-arid to arid climates and different clayey soils. While the magnitudes of stress and deformation may vary depending on soil properties and climatic conditions, the fundamental mechanisms described in the manuscript remain valid and consistent. However, conducting a sensitivity analysis of the results across a wide range of environmental conditions, from extreme dryness to wet processes and various soil types, is beneficial.

While soils often reach an equilibrium state after several wetting-drying cycles, where crack depth stabilizes and only minor changes in crack width occur, the fixed crack depth in the simulations introduces certain simplifications. In natural systems, cracks may propagate to variable depths before stabilizing, affecting subsurface stress redistribution, volumetric behavior, and pore water pressure. Additionally, the evaporation rate and associated soil swelling and shrinkage are influenced by the interplay between environmental conditions and evolving crack geometry. By fixing crack depth, the model may underestimate or oversimplify the dynamic feedback between crack depth and surface processes. Despite this limitation, the model is capable of identifying the deformed crack geometry at each time step. It also takes into account the changes in crack width and internal area on the interaction of parameters such as stress, strain, and pore water pressure. Nonetheless, the findings are most applicable to scenarios where crack depth remains relatively stable, such as in soils with deep groundwater level.

Future studies should adopt new methods to examine the propagation of crack depth and the potential initiation of new cracks during wetting-drying cycles. Additionally, the geometry of cracks involves several complexities. Previous studies have indicated that the shape of cracks in a 3D view exhibits various characteristics, including width, depth, length, inclination, the number of crack segments, crack intensity factor (CIF), and the number of intersections. A 3D model could also be utilized to explore the characteristics of the 3D crack network in relation to the soil surface deformation mechanism. Furthermore, secondary cracks, branching, and complex crack network interactions are not explicitly represented, yet these features are vital for understanding subsurface connectivity and deformation mechanisms. Multi-scale models that capture both primary and secondary cracks are needed. Moreover, the inclusion of soil-root-atmosphere interactions affects crack initiation and propagation mechanism and pore water pressure distribution. Incorporating such interactions would provide a holistic understanding of soil behavior under natural conditions. Hence, addressing these limitations will significantly enhance the understanding of desiccation-cracked soils and broaden the applicability of the findings to a wider range of environmental and engineering scenarios.

7. Conclusions

This study investigated the thermo-hydro-mechanical behavior of desiccation-cracked soils under cyclic wetting-drying conditions, emphasizing stress redistribution, pore volume evolution, and crack mechanics.

Over three years, total porosity and micro-porosity exhibited a progressive decrease, with micro-porosity reducing from 0.126 to 0.067 at suction levels of 50–150 MPa in the first year. By the third year, a 22% reduction in total porosity was observed, indicating a gradual shift toward an equilibrium state. The maximum plastic strain increased from 16.8% in the first year to 19.7% in the third year, demonstrating the irreversible nature of shrinkage-induced deformation.

Stress redistribution patterns showed strong correlations with climate-driven moisture variations. During wetting, compressive horizontal stresses developed at crack tips due to swelling, with stress increasing by 5.22 times its initial value. Concurrently, compressive principal stresses along crack edges intensified by 7.55 times compared to the initial stress state. During drying, tensile stresses dominated, particularly at the crack walls and tip, facilitating crack propagation.

The results further demonstrate that both tensile and shear stress-induced cracking mechanisms contribute to soil deformation. Shear stress increased significantly with rising soil moisture during rainfall and decreased during drying cycles. The findings revealed that during wetting, crack walls experienced shear stress localization, which facilitated particle mobilization along crack surfaces and shear-induced displacement. The alternation of positive and negative shear stress along crack edges indicated shear-induced crack widening, particularly at the upper edges of deep cracks, where failure occurred along the wetting path.

The results of fracture mechanics analysis demonstrate that under wetting conditions, rainfall infiltration reduces tensile stress, leading to negative K_I values as low as -3.9 kPa $m^{1/2}$, indicating crack closure due to compressive stresses. Conversely, under high temperatures, desiccation-induced shrinkage increases tensile stress, elevating K_I to 1.43 kPa $m^{1/2}$ at the crack tip, promoting crack propagation. The G_I provides a measure of the available energy for fracture extension. The highest G_I values, reaching 63 mJ/m^2 under rainfall and 8.6 mJ/m^2 under drying conditions, are consistently observed at the crack tip, reinforcing

its role as the primary location for fracture growth. These findings highlight that the crack tip is the most vulnerable region for propagation due to stress concentration and energy accumulation, while the crack edge is particularly susceptible to degradation due to direct exposure to environmental loading.

CRediT authorship contribution statement

Milad Jabbarzadeh: Writing – original draft, Visualization, Validation, Software, Methodology, Investigation, Conceptualization. **Hamed Sadeghi:** Writing – review & editing, Supervision, Methodology, Conceptualization.

Data availability statement

The data that support the findings of this study are available from the corresponding author upon reasonable request.

Declaration of competing interest

The authors declare that they have no known competing financial interests or personal relationships that could have appeared to influence the work reported in this paper.

Acknowledgements

The financial support provided by the Research Grant Office at Sharif University Technology by way of grants G4010902 and QB020105 is gratefully acknowledged.

References

Abu-Hejleh, A.N., Znidarčić, D., 1995. Desiccation theory for soft cohesive soils. J. Geotech. Eng. 121 (6), 493–502.
Alonso, E.E., Vaunat, J., Gens, A., 1999. Modelling the mechanical behaviour of expansive clays. Eng. Geol. 54 (1–2), 173–183.
Bernier, F., Li, X.L., Bastiaens, W., 2007. Twenty-five years' geotechnical observation and testing in the tertiary boom clay formation. Geotechnique 57 (2), 229–237.
Cuisinier, O., Laloui, L., 2005. Fabric evolution of an unsaturated compacted soil during hydromechanical loading. In: Unsaturated Soils: Experimental Studies. Proceedings of the International Conference "From Experimental Evidence Towards Numerical Modeling of Unsaturated Soils,". Springer, Berlin Heidelberg,Weimar, Germany.
De Bruyn, D., Labat, S., 2002. The second phase of ATLAS: the continuation of a running THM test in the HADES underground research facility at. Mol. Eng. Geol. 64 (2–3), 309–316.
Dehandschutter, B., Vandycke, S., Sintubin, M., Vandenberghe, N., Wouters, L., 2005. Brittle fractures and ductile shear bands in argillaceous sediments: inferences from Oligocene boom clay (belgium). J. Struct. Geol. 27 (6), 1095–1112.
Delage, P., Sultan, N., Cui, Y.J., 2000. On the thermal consolidation of boom clay. Can. Geotech. J. 37 (2), 343–354.
François, B., Laloui, L., Laurent, C., 2009. Thermo-hydro-mechanical simulation of ATLAS in situ large scale test in boom clay. Comput. Geotech. 36 (4), 626–640.
Fredlund, D.G., Rahardjo, H., 1993. Soil Mechanics for Unsaturated Soils. John Wiley & Sons.
Gambolati, G., Teatini, P., 2015. Geomechanics of subsurface water withdrawal and injection. Water Resour. Res. 51 (6), 3922–3955.
Gens, A., Alonso, E.E., 1992. A framework for the behaviour of unsaturated expansive clays. Can. Geotech. J. 29 (6), 1013–1032.
Gens, A., Vaunat, J., Garitte, B., Wileveau, Y., 2011. In situ behaviour of a stiff layered clay subject to thermal loading: observations and interpretation. In: Stiff Sedimentary Clays: Genesis and Engineering Behaviour. Géotechnique Symposium in Print 2007. Thomas Telford Ltd, pp. 123–144.
Ghandilou, M.J., Tourchi, S., Sadeghi, H., 2023. Numerical investigation of cyclic wetting and drying of boom clay based on the Barcelona expansive model. In: 84th EAGE Annual Conference & Exhibition, vol 2023. European Association of Geoscientists & Engineers, pp. 1–5, 1.
Guo, L., Chen, G., Ding, L., Zheng, L., Gao, J., 2023. Numerical simulation of full desiccation process of clayey soils using an extended DDA model with soil suction consideration. Comput. Geotech. 153, 105107.
Haghighat, N., Sattari, A.S., Wuttke, F., 2023. Finite discrete element modeling of desiccation fracturing in partially saturated porous medium. Comput. Geotech. 164, 105761.
Houcem, T., Alassaf, Y., Jamei, M., Olivella, S., 2023. Desiccation cracks prediction using a 3D finite elements model. Int. J. Geotech. Eng. 17 (2), 162–176.
Jabbarzadeh, M., Sadeghi, H., 2024. A novel analytical-statistical-numerical hybrid framework for investigating the thermo-hydro-mechanical behavior of heterogeneous subsidence phenomena, moisture and temperature variations in cracked soils under soil-atmosphere interaction. Sharif J. Mech. Eng. https://sjme.journals.sharif.edu/article_23776.html?lang=en.
Jabbarzadeh, M., Sadeghi, H., Tourchi, S., Darzi, A.G., 2024. Thermo-hydraulic analysis of desiccation cracked soil strata considering ground temperature and moisture dynamics under the influence of soil-atmosphere interactions. Geomech. Energy Environ. 38, 100558.
Knott, J.F., 1973. Fundamentals of Fracture Mechanics. Gruppo Italiano Frattura.
Konrad, J.M., Ayad, R.J.C.G.J., 1997. Desiccation of a sensitive clay: field experimental observations. Can. Geotech. J. 34 (6), 929–942.
Kolahdooz, A., Sadeghi, H., Ahmadi, M.M., 2020. A numerical study on the effect of salinity on stability of an unsaturated railway embankment under rainfall. In: E3S Web of Conferences, vol. 195. EDP Sciences, 01004.
Li, C., Kong, L., An, R., 2022. Evolution of cracks in the shear bands of granite residual soil. J. Rock Mech. Geotech. Eng. 14 (6), 1956–1966.
Lu, Y., Liu, S., Weng, L., Wang, L., Li, Z., Xu, L., 2016. Fractal analysis of cracking in a clayey soil under freeze–thaw cycles. Eng. Geol. 208, 93–99.
Morris, P.H., Graham, J., Williams, D.J., 1992. Cracking in drying soils. Can. Geotech. J. 29 (2), 263–277.
Mousavi, Z., Jabbarzadeh, M., 2025. 3D DEM-Based analysis of cylindrical rock specimen failure and micro-fracturing: impact of stiffness and tensile strength. Discover Geosci 21.
Mualem, Y., 1976. A new model for predicting the hydraulic conductivity of unsaturated porous media. Water Resour. Res. 12 (3), 513–522.
Nowamooz, H., Masrouri, F., 2008. Hydromechanical behaviour of an expansive bentonite/silt mixture in cyclic suction-controlled drying and wetting tests. Eng. Geol. 101 (3–4), 154–164.
Olivella, S., Gens, A., Carrera, J., Alonso, E.E., 1996. Numerical formulation for a simulator (CODE_BRIGHT) for the coupled analysis of saline media. Eng. Comput. 13 (7), 87–112.
Panday, S., Corapcioglu, M.Y., 1989. Reservoir Transport Equations by Compositional Approach, vol. 4. Transport Porous Media, pp. 369–393.
Romero, E., 1999. Characterisation and thermal-hydro-mechanical Behaviour of Unsaturated Boom Clay: an Experimental Study. Ph.D. Thesis. Technical University of Catalonia, Spain.
Sadeghi, H., Chiu, A.C., Ng, C.W., Jafarzadeh, F., 2020. A vacuum-refilled tensiometer for deep monitoring of in-situ pore water pressure. Sci. Iran. 27 (2), 596–606.
Sadeghi, H., Jabbarzadeh, M., Tourchi, S., 2024. Thermo-hydro-mechanical modelling of the heterogeneous subsidence and swelling in the desiccation cracked clayey strata. Eng. Geol., 107798
Sadeghi, H., Darzi, A.G., Voosoghi, B., Garakani, A.A., Ghorbani, Z., Mojtahedi, S.F.F., 2023. Assessing the vulnerability of Iran to subsidence hazard using a hierarchical FUCOM-GIS framework. Remote Sens. Appl.: Soc. Environ. 31, 100989.
Sánchez, M., Gens, A., do Nascimento Guimarães, L., Olivella, S., 2005. A double structure generalized plasticity model for expansive materials. Int. J. Numer. Anal. Methods GeoMech. 29 (8), 751–787.
Tang, C.S., Cheng, Q., Gong, X., Shi, B., Inyang, H.I., 2023. Investigation on microstructure evolution of clayey soils: a review focusing on wetting/drying process. J. Rock Mech. Geotech. Eng. 15 (1), 269–284.
Tang, C.S., Cheng, Q., Lin, L., Tian, B.G., Zeng, H., Shi, B., 2022. Study on the dynamic mechanism of soil desiccation cracking by surface strain/displacement analysis. Comput. Geotech. 152, 104998.
Tang, C.S., Cui, Y.J., Tang, A.M., Shi, B., 2010. Experiment evidence on the temperature dependence of desiccation cracking behavior of clayey soils. Eng. Geol. 114 (3–4), 261–266.
Tian, B.G., Cheng, Q., Tang, C.S., Shi, B., 2023. Healing behaviour of desiccation cracks in a clayey soil subjected to different wetting rates. Eng. Geol. 313, 106973.
Tourchi, S., Jabbarzadeh, M., Sadeghi, H., 2024b. Thermo-hydro-mechanical analysis of soil strata suffered from desiccation cracking. In: Geotechnical Engineering Challenges to Meet Current and Emerging Needs of Society. CRC Press, pp. 1362–1367.
Tourchi, S., Jabbarzadeh, M., Lavasan, A.A., Sadeghi, H., Racek, O., 2024a. Thermo-hydro-mechanical dynamics of a rock slope: integrated field and numerical analysis at the požáry test site in the Czech Republic. J. Rock Mech. Geotech. Eng.
Towner, G.D., 1987. The mechanics of cracking of drying clay. J. Agric. Eng. Res. 36 (2), 115–124.
Valipour, M., Jabbarzadeh, M., Sadeghi, H., Roghangar, K., 2024. Volumetric behavior of a soil column subjected to freeze-thaw cycles under coupled thermo-hydro-mechanical conditions. GeoMontréal 2024. https://www.researchgate.net/publication/384431981.
Van Genuchten, M.T., 1980. A closed-form equation for predicting the hydraulic conductivity of unsaturated soils. Soil Sci. Soc. Am. J. 44 (5), 892–898.
Wang, G., Wei, X., 2015. Modeling swelling–shrinkage behavior of compacted expansive soils during wetting–drying cycles. Can. Geotech. J. 52 (6), 783–794.
Wang, Q., Tang, A.M., Cui, Y.J., Barnichon, J.D., Ye, W.M., 2013. Investigation of the hydro-mechanical behaviour of compacted bentonite/sand mixture based on the BExM model. Comput. Geotech. 54, 46–52.
Wang, X., Yu, J., Li, Q., Yu, Y., Lv, H., 2022. Study on the crack evolution process and stress redistribution near crack tip in soil. Int. J. GeoMech. 22 (1), 04021255.
Wei, X., Hattab, M., Bompard, P., Fleureau, J.M., 2016. Highlighting some

mechanisms of crack formation and propagation in clays on drying path. Geotechnique 66 (4), 287–300.
Wheeler, S.J., Sharma, R.S., Buisson, M.S.R., 2003. Coupling of hydraulic hysteresis and stress–strain behaviour in unsaturated soils. Geotechnique 53 (1), 41–54.
Xu, J.J., Tang, C.S., Cheng, Q., Xu, Q.L., Inyang, H.I., Lin, Z.Y., Shi, B., 2022. Investigation on desiccation cracking behavior of clayey soils with a perspective of fracture mechanics: a review. J. Soils Sediments 1–30.
Xu, X.T., Liu, D.Q., Xian, Z.X., Yang, F., Jian, W.B., Xu, X., Huang, J.B., 2022. Influence of drying–wetting cycles on the water retention and microstructure of residual soil. Geofluids 2022 (1), 9948658.
Yu, Z., Eminue, O.O., Stirling, R., Davie, C., Glendinning, S., 2021. Desiccation cracking at field scale on a vegetated infrastructure embankment. Géotech. Lett. 11 (1), 88–95.
Zeng, H., Tang, C.S., Zhu, C., Vahedifard, F., Cheng, Q., Shi, B., 2022. Desiccation cracking of soil subjected to different environmental relative humidity conditions. Eng. Geol. 297, 106536.
Zhou, C., Ng, C.W.W., 2016. Effects of temperature and suction on plastic deformation of unsaturated silt under cyclic loads. J. Mater. Civ. Eng. 28 (12), 04016170.

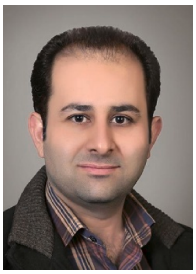

Hamed Sadeghi is Associate Professor of Civil and Environmental Engineering at Sharif University of Technology. He holds an impressive array of academic degrees, with notable distinctions recognized by Iran's National Elites Foundation. Hamed is pioneering innovative programs, serving as the first graduate and coordinator of the SUT-HKUST Dual-Degree PhD program. He is the director of the Geotechnical Group and the founding director of the Green Geotechnology Laboratory. Hamed has been the recipient of numerous awards, including the KANS honorary diploma, the "Dr. Kazemi-Ashtiani" prize, the best PhD thesis, as well as being named Sharif University's distinguished research scholar for international collaborations having over 90 publications. He has served as the Chair of the Iran InterPore Chapter and the Chair of TC-106 Unsaturated Soils, of the Iranian Geotechnical Society. His research team is at the forefront of advancing knowledge about the complex interplay between soil, solutes, atmosphere, and plants.